NTNU

Norwegian University of
Science and Technology

Electromagnetic Modelling and Inversion of Seafloor Massive Sulphide Deposits

Imaging of SMS Deposits and the Asthenosphere at the Atlantic Mid-Ocean Ridge

Jonas Fagerli Tegnander

Petroleum Geoscience and Engineering
Submission date: June 2017
Supervisor: Ståle Emil Johansen, IGP
Co-supervisor: Martin Panzner, EMGS

Norwegian University of Science and Technology
Department of Geoscience and Petroleum

Summary

Seafloor massive sulphides (SMS) are seen as an increasingly important mineral resource for the future. Fewer mineral discoveries are being made in the shallow subsurface onshore, and therefore a more petroleum related approach will be used in order to explore for mineral ores at greater depths. With electromagnetics (EM) being frequently used for decades in subsurface imaging, and recent years with controlled source electromagnetics (CSEM) for hydrocarbon exploration, marine CSEM could be used to detect conductive anomalies in the mineral deposits at the ocean floor. In this thesis, the objective was to investigate if it is possible to image SMS with marine CSEM through synthetic forward modelling and inversion with structured and unstructured grids in MARE2DEM. It was also tested how well marine magnetotelluric (MT) and marine CSEM was able to image a mantle structure beneath the mid-ocean ridge through modelling and inversion.

Survey geometry and parameters were set up before creating a start model in order to generate synthetic data through forward modelling. Noise was added to the data before a simple inversion model with refined rectangular and triangular grids was created. Through inversion, a resistivity model as close to the start model as possible was generated in MARE2DEM.

From changing parameters, such as frequency, receiver spacing, and mineral mound sizes, in the modelled CSEM survey and inversion it was found that buried SMS deposits must be of a significant size in order to be detected and that high frequencies and shorter receiver spacing enhance the geophysical response of the deposits. For mineral mounds found on the seabed, smaller geometries could be detected.

Sammendrag

Massive sulfider på havbunnen blir i økt grad sett på som en mulig mineralkilde for fremtiden. Med færre landlige mineralfunn på grunt dyp, vil en mer petroleumsrelatert tilnærming til leting etter dypere mineralårer bli brukt. Elektromagnetiske metoder har i flere tiår blitt brukt til avbildning av undergrunnen og i de siste årene til leting etter hydrokarboner ved hjelp av CSEM (Controlled Source Electromagnetics). Med marin CSEM bør det derfor være mulig å oppdage konduktive anomalier i mineralforekomstene på havbunnen. I denne masteroppgaven vil hovedfokuset være å undersøke om det er mulig å avbilde de massive sulfidene med marin CSEM ved bruk av syntetisk forovermodellering og inversjon med strukturerte og ustrukturerte inversjonsgrid i MARE2DEM. Oppgaven tar for seg også hvor godt det var mulig å avbilde en mantelstruktur under midthavsryggen ved bruk av marin magnetotelluric metode og marin CSEM gjennom syntetisk forovermodellering og inversjon.

Før startmodellen ble laget, ble innsamlingsgeometrien og hvilke parametre som skulle bli brukt bestemt for å kunne generere syntetiske data ved hjelp av forovermodellering. Så ble støy lagt til dataene, før en enkel inversjonsmodell med rektangulære og triangulære grids ble laget. Gjennom inversjon ble en resistivitetsmodell generert gjennom flere iterasjoner, for å komme så nærme startmodellen som mulig, i MARE2DEM.

Ved å bytte parametre i forovermodellen og i inversjonen som frekvens, mottakeravstand og størrelse på mineralforekomstene, ble det kommet fram til at de sedimentbegravde massive sulfidforekomstene må være av betydningsfull størrelse for å kunne bli oppdaget. Høye frekvenser og kortere mottakeravstand forsterker den geofysiske responsen til avsetningene. For mineralforekomstene lokalisert på havbunnen kunne mindre mineralgeometrier bli oppdaget.

Preface

This report is the result of my master thesis at the Norwegian University of Science and Technology (NTNU) in the course *Petroleum Geosciences, Master Thesis - TPG4925* with specialisation within geophysics and completes my five years at NTNU. The thesis is about electromagnetic modelling and inversion of seafloor massive sulphides at the mid-ocean ridge and was chosen together with my supervisor. It is a continuation of the specialisation project that was carried out last semester, and some of the geometries that are used in the thesis are from that project. It is recommended that readers have a basic understanding of geology and geophysics.

Trondheim 11.06.17
Jonas Fagerli Tegnander

Acknowledgements

I would like to thank Electromagnetic Geoservices (EMGS) for letting me write this thesis with their help and letting me use their training material for illustrations. I sincerely thank my supervisor Ståle Emil Johansen for accepting to be my supervisor and providing such an interesting topic for my to work with the last year through the specialisation project and this thesis. Also, many thanks to Eirik Vik for great feedback and discussions regarding this thesis, and to Anna Lim for help and good discussions during the last year.

I wish to express my sincere gratitude to my co-supervisor Martin Panzner at EMGS who has given me extraordinary help all the way through this thesis. He has taught me everything I know of the software that has been used to provide the results, and for the great feedback on the writing part of this thesis. Thank you so much for using your valuable time to help me with my final thesis and for the close follow-up that you have given me all semester.

I would also like to thank NTNU and my fellow students for five good years, as well as an incredible semester abroad in Sydney at UNSW.

Table of Contents

List of Tables

List of Figures

Abbreviations

AMOR	=	Atlantic Mid-Ocean Ridge
AUV	=	Autonomous Underwater Vehicle
CSEM	=	Controlled Source Electromagnetic
EM	=	Electromagnetic
HED	=	Horizontal Electrical Dipole
IP	=	Induced Polarization
MT	=	Magnetotelluric
MvO	=	Magnitude versus Offset
PvO	=	Phase versus Offset
RMS	=	Root Mean Square
SMS	=	Seafloor Massive Sulphides
TAG	=	Trans-Atlantic Geotraverse
TE	=	Transverse Electric
TM	=	Transverse Magnetic

Chapter 1

Introduction

There has been an increased interest in marine mineral exploration in the recent years. In the last 60 years, the majority of the marine mineral discoveries are found in the shallow subsurface, within the upper 50 m onshore. Onwards, fewer discoveries will be made in the shallow subsurface onshore, and therefore a more petroleum related technology will be used in order to explore efficiently (Witherly, 2012). It is just in the recent decades that marine mineral exploration has been used to find prospects suitable for mining offshore. The petroleum technologies used in hydrocarbon exploration, and for deep mineral exploration onshore, will be eminent for mineral exploration offshore in the future.

Electromagnetic signals have for decades been frequently applied to imaging and mapping of subsurface resistivity structures. Electromagnetic detection and characterization of hydrocarbon bearing reservoirs offshore were introduced with Statoil's Sea Bed Logging from 2002 (Eidesmo et al., 2002). Marine controlled source electromagnetic (CSEM) sounding was leading way for an alternative approach to hydrocarbon detection.

Hydrocarbons are highly resistive in contrast to brine filled sediments which are rather conductive. It is, therefore, possible to identify hydrocarbon accumulations using marine CSEM. Marine minerals, on the contrary, has very low resistivity, or high conductivity, and will like hydrocarbons produce a resistive anomaly that could be detected. The purpose of this thesis is to investigate if it is possible to detect and image SMS with marine CSEM. Synthetic forward modelling and inversion will be used to investigate the feasibility of this technology. It will therefore only be given a brief introduction to what SMS deposits are and how they are formed. How well a deep magma chamber in the asthenosphere is possible to image with marine MT and marine CSEM is also to be investigated. The models are conceptual but realistic, and they are made with the main focus on forward modelling and inversion and how well it is possible to image these structures.

Seafloor massive sulphides (SMS) deposits are seen as an increasingly important marine mineral resource for the future. There is a growing number of industrialised nations that are involved in surveying and drilling after samples of such deposits. The electrical properties of the deposits are distinguishable from their unmineralized host rocks (Spagnoli et al., 2016; Petersen et al., 2016). They range in size from only few meters in diameters to those at TAG (Transatlantic Geotraverse), which reach 250 m in diameter and up to 50 m in height (Petersen et al., 2000), and all the way to ore bodies in Manus Basin north

of Papua New Guinea which consists of a mound 2 km in diameter rising 200 m above the seafloor (Boschen et al., 2013).

The electric properties used in this study for the SMS deposits, volcanic basement, magma chamber, and sediments are not taken from samples, but from literature discussing similar topics with similar geological features (Key et al., 2013; Spagnoli et al., 2016). The tests are also done in two-dimensional space, where the model properties vary along the observation plane and in depth (R(x,z). The models are assumed to be invariant normal to the observation plane. Also, in this study, a simplification assumption is made that the model properties are isotropic.

Chapter 2

Theory

In this chapter, it will be given a brief introduction to what seafloor massive sulphides (SMS) are, where they may be found as well as how they are formed. It will also be discussed two different electromagnetic methods, the marine magnetotelluric (MT) method and the marine controlled source electromagnetic (CSEM) method. The focus for the methods will be some basics of how they work, why they work and some data examples will be given. The last part of this chapter will be on electromagnetic inversion theory, what it is and how it is used to generate results.

2.1 Seafloor Massive Sulphides

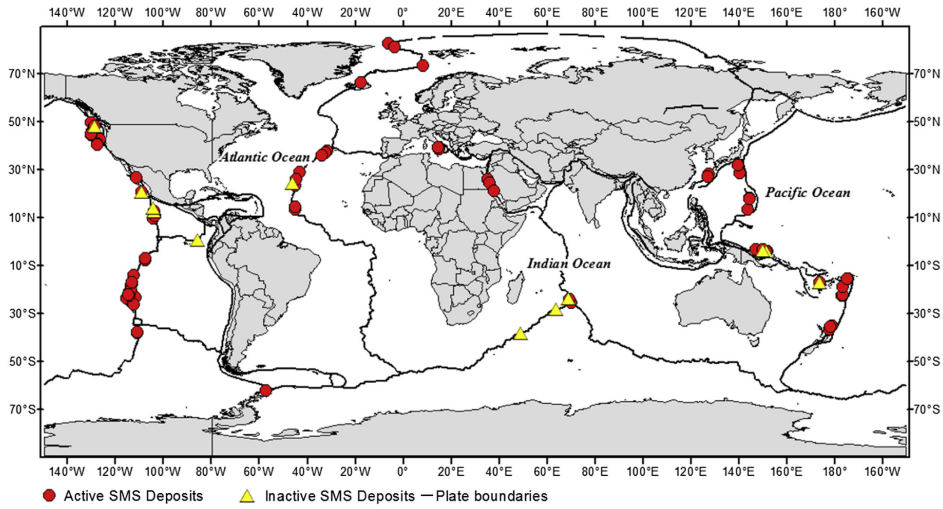

Figure 2.1: Map of the global distribution of SMS deposits and where they are located around the world. Red circles indicates active SMS deposit sites, and the yellow triangles indicates where the inactive SMS deposits are found. The black bold line indicates plate boundaries. Modified from Boschen et al. (2013)

Seafloor massive sulphides (SMS) are found as strata bound accumulations of sulphide minerals at or near the seafloor that has precipitated from high-temperature hydrothermal activity. It is associated with seafloor volcanism, and form as a result of the mixing of hot metal-rich hydrothermal fluids with the cold seawater (Spagnoli et al., 2016; Shanks and Thurston, 2012). Deep-sea mining of SMS deposits is a new potential source of Cu, Zn, Au and Ag (Glasby, 2002; Hoagland et al., 2010; Hekinian, 2014).

SMS are mostly found along global mid-ocean ridges, submarine volcanic arcs and in rifted back-arc basins behind active subduction zones (Shanks and Thurston, 2012; Spagnoli et al., 2016). **Fig. 2.1** shows the global distribution of SMS deposits around the world.

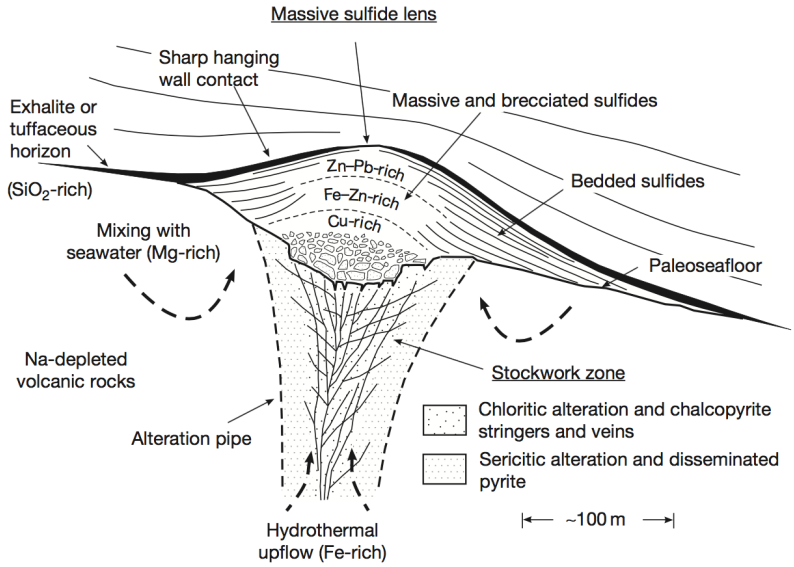

Figure 2.2: The structure of an SMS deposit. Schematic cross-section of a SMS deposit. Showing zonation within the mound and stockwork zone in the alternation pipe. Black dashed arrows indicates fluid flow. Modified from Hannington (2014)

The SMS deposits are found when dissolved metals in the hydrothermal fluids are expelled at black and white smokers vents, or focused flows and diffuse flows respectively. The metal minerals will also grow into ”chimneys” around the vents and into larger mounds of chimney debris. Most deposits are characterised by internal zoning of the minerals, with Cu-dominant sulphides at the internal base and with Zn- or Pb-rich sulphides at the top and outer margins (Hannington, 2014) as seen in **Fig. 2.2**. In the underlying parts of the deposit, where the hydrothermal fluids have passed through, a network of sulphides has developed in the volcanic rocks. **Fig. 2.2** shows this ”stockwork” zone where veins of sulphides in a matrix of chemically altered host rock have formed.

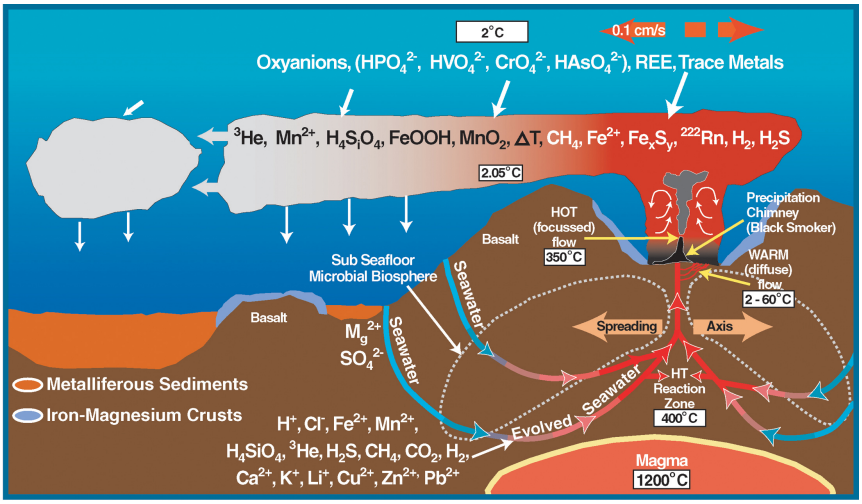

Figure 2.3: The chemical circulations around and at a black smoker complex. Cold seawater (blue arrows) descends through faults and fissures towards the magma heat source while leaching minerals from the host rock. Heated seawater (red arrows) rise with metal mineral content towards the seafloor and are precipitated through a black smoker (hot concentrated) or a white diffuse smoker (warm). Modified from NOAA (05.06.17)

Hydrothermal activity is a by-product of volcanism, and it is the alternation of rocks due to the circulation of hot fluids in the lithosphere. It causes precipitation of metallic minerals such as Cu, Fe, Pb, Zn-sulphides, Ag and Au (Hekinian, 2014). **Fig. 2.3** illustrates how cold seawater penetrates the rocks beneath the seafloor through fissures, cracks, and pores as it descends through the lithosphere until it reaches a heat source which causes it to react with the surroundings (Shanks and Thurston, 2012; Hekinian, 2014).

The circulation system can be described as four different zones: The recharge zone, the acidification zone, the reaction zone and the discharge zone. The recharge zone is where the cold seawater is drawn into the crust in the down-flowing limb of the hydrothermal convection cell (Hannington, 2014; Shanks and Thurston, 2012; Hekinian, 2014). In **Fig. 2.4** this can be seen as the cold seawater descends through the dyke section down towards the reaction zone. On the way towards the reaction zone, however, it reaches the acidification zone. In the acidification zone, the loss of Mg^{2+} from the seawater makes it more acidic and therefore more corrosive. As the seawater descends, it will eventually be in the proximity of the heat source, such as a magma chamber. This transition from the acidification zone to the reaction zone can be seen in **Fig. 2.3** as "evolved seawater". The deepest part of the circulation system is the reaction zone and it is where the temperature of the fluids will rise as it approaches the heat source, which may be situated anywhere between 0.5-2 km within the crust. The reaction zone has a temperature of 390-400 ^{o}C, and dissolution of minerals occur as the fluids are progressively heated and reaching equilibrium with the altered host rock (Hannington, 2014). After passing through this hot part of the convective system, the hydrothermal fluids rise buoyantly along a high permeability zone of dykes and deeply penetrating synvolcanic faults towards the seafloor. The discharge

zone is where the hydrothermal hot fluids react with the ambient seawater and discharge the leached metals from the underlying rocks onto the seafloor. The magma chamber itself may also contribute with metal minerals (Yang and Scott, 1994).

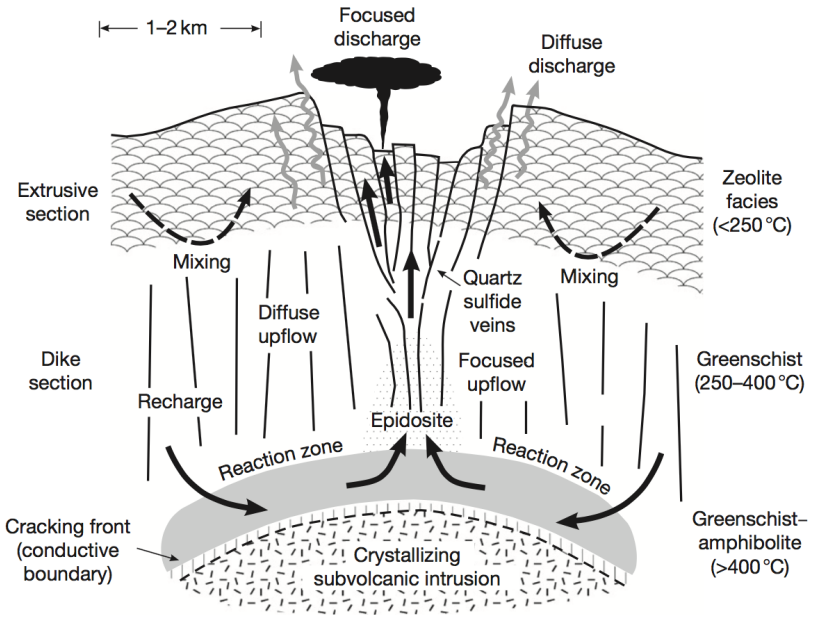

Figure 2.4: A model of a typical submarine hydrothermal system at a mid-ocean ridge which illustrates the relationships between the recharge zone, reaction zone and the discharge zone. Modified from Hannington (2014)

Transition metals such as Cu, Zn, Fe, Mn, Ag, and Au are the most likely metals to leach and form compounds with sulphur and chlorine. The hydrothermal fluids that are exiting the chimneys at the seafloor are found in concentrated jets of only a few centimetres in diameter. As the vent fluid is discharged it is diluted by the seawater and creates a hydrothermal plume that rises above the seafloor. This plume rises a couple of hundred meters above the seafloor before it reaches the density of the ambient seawater (Hekinian, 2014).

From **Fig. 2.3**, one can see that the metal minerals are deposited on different locations around the venting site. From deposition from the plume, but also from within the discharge zone, **Fig. 2.2** e.g. as a stockwork zone. The formation of the metalliferous deposits can be described in five different stages. The first stage involves the discharge of low temperature ($<150\ ^{o}$C) fluids through pillow lavas and sheet flows, depositing iron silicates and some sulphides. On site, this will be host for a gathering of the benthic animal community, which includes tube worms and clams. The high temperature ($>350\ ^{o}$C) fluid discharge makes up the next stage and is where the construction of the chimneys takes place. The chimney channel the fluids and are the provoking factor for precipitation of iron-copper sulphides and anhydrite. An accumulation of several chimney structures leads

to the development of a mound, where even more hydrothermal fluids can filtrate through the lithosphere, precipitating iron-copper-zink sulphides. In this stage, the stockwork is formed from circulation of the hydrothermal fluids and the alteration of the host rock together with precipitation of metalliferous compounds. As the fluids starts to cool again, hydrothermal fluids with temperature below 200 ^{o}C will be discharged and form mineral compounds that will fill the pores and fissures of the mound, creating a zonal distribution of minerals with copper centered, and with zinc and iron sulphide towards the outer bounds of the mound (Hekinian, 2014). The final stage happens during tectonic events. Formation of normal faulted scraps will occur and can expose the stockwork and a talus of slumped material will gather at the foot.

Table 5
Seafloor massive sulfide occurrences for which size information is available based on drilling information. Abbreviations: ODP=Ocean Drilling Program; ROV=remotely-operated vehicle.

Deposit	Location	Size	Drilling tool/ vessel	Reference
Atlantis II	Red Sea	90 Mt	Coring	[47]
Middle Valley	Juan de Fuca Ridge	10–15 Mt	ODP-drill ship	[50]
TAG	Mid-Atlantic Ridge	4 Mt	ODP-drill ship	[49,54]
Izena	Okinawa Trough	3.4 Mt	Lander-type	[57]
Solwara 1	Bismarck Sea	2.5 Mt	ROV-based	[56]
Solwara 12	Bismarck Sea	0.2 Mt	ROV-based	[56]
Fryer, Pika	Mariana Trough	Small	Lander-type	[58]
Iheya North	Okinawa Trough	Small	IODP-drill ship	[55]
Logatchev	Mid-Atlantic Ridge	Small	Lander-type	[31]
PacManus	Bismarck Sea	Small	ODP-drill ship	[51]
PacManus	Bismarck Sea	Small	Lander-type	[52]
Palinuro	Tyrrhenian Sea	Small	Lander-type	[53]
Suiyo	Izu-Bonin Arc	Small	Lander-type	[59]

Figure 2.5: Table of some drilled SMS deposits, where they are located, and the size of the deposits. Modified from (Petersen et al., 2016).

While the number of discoveries of SMS deposits is increasing, most deposits are small in comparison to their land-based analogues. The hydrothermal venting systems are also inefficient, as a lot of the metal content is lost to the hydrothermal plumes and dispersed away from the vent site. SMS deposits vary in size from a few tonnes to above 20 Mt of sulphide material (Petersen et al., 2016). **Fig. 2.5** shows an overview of drilled SMS deposits, their location, and their size. In most cases is the size of the deposits estimated from visual observations and not drilling. **Fig. 2.5**, however, is from drilling. The individual chimneys vary in size as well, from a few centimetres and up to 45 m in height. They collapse over time and accumulate as mounds which contain a major part of the metal content in the deposits (Petersen et al., 2016). One of the largest SMS deposits is found at the Mid-Atlantic Ridge. The TAG (Trans-Atlantic Geotraverse) hydrothermal

mound which measures 200 m in diameter and 50 m high and contains approximately 3.9 million tonnes of sulphide bearing-material (Petersen et al., 2000).

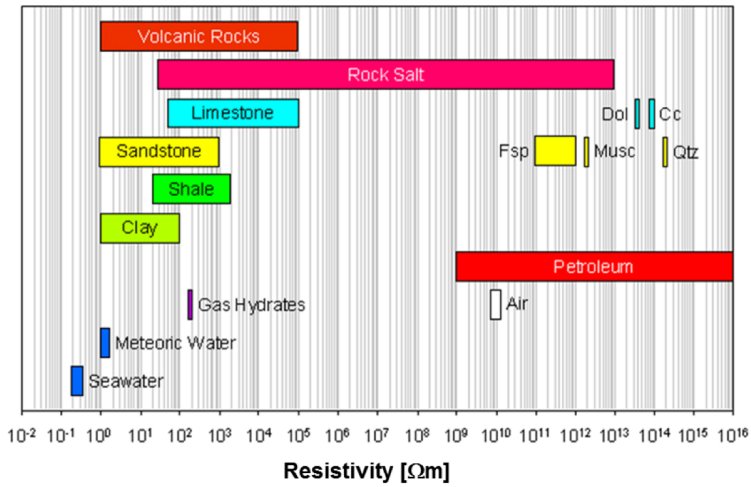

Figure 2.6: The different resistivity values of some minerals and rock types (EMGS training material).

The most common minerals present in SMS are Fe-minerals such as pyrite and pyrrhotite, the commercially interesting Cu-sulphide mineral chalcopyrite and the Zn-sulphide mineral sphalerite (Hekinian, 2014; Spagnoli et al., 2016). Minor amounts of galena, tetrahedrite, tennantite, arsenopyrite, bornite, and magnetite can are also associated with SMS deposits. About 20-40% of the mined minerals are so called gangue minerals, which are non-commercial minerals, mainly silicates, that are coprecipitated with the sulphide minerals or formed by alteration of the host rocks (Hannington, 2014).

Fig. 2.6 illustrates the different resistivity values for some rocks and minerals. Electrical conductivity describes how well a material allows electrical currents to pass through it, and a typical sedimentary rock will consist of solid rock matrix and pore space that may be filled with either fluids (seawater or hydrocarbons) or secondary minerals, for a marine case (Spagnoli et al., 2016). The relationship between resistivity (ρ) and conductivity (σ) is:

$$\rho = \frac{1}{\sigma} \tag{2.1}$$

For sediments, there is a good correlation between pore-fluid resistivity, porosity and the total resistivity of the sample, which can be summarised by Archie's law:

$$\rho_b = a\rho_w\phi^{-m} \tag{2.2}$$

where ρ_b is the rock resistivity, ρ_w the pore fluid resistivity, ϕ the porosity of the rock, whilst m is the cementation exponent of the rock and a is related to tortuosity. But, in Archie's law, the matrix is considered an electrical insulator rather than a conductor. For

SMS deposits, many of the minerals are electrically conducting, which means Archie's law does not apply for SMS deposits, and the bulk resistivity will depend in much larger scale on the conductivity of the minerals (Spagnoli et al., 2016). In this case then, the electrical resistivity must be described by a complex number as a function of frequency. The frequency is expressed by the amplitude and phase function:

$$\rho^*(f) = |\rho| e^{i\phi(f)} \tag{2.3}$$

where * denotes the complex value and i is the imaginary unit. Since it is an frequency dependent resistivity it can be used to separate sulphide-rich deposits from unmineralized samples. In this study however, low frequencies are used and frequency dependancy is small and negligible. A typical host rock can be a massive basalt, which may reach resistivities up to 10 000 Ωm, but more porous basalts can be in the range of a few Ωm to tens of Ωm (Spagnoli et al., 2016). Rocks that has been hydrothermally altered and SMS deposits with high sulphide and clay contents are characterized by lower resistivity values around a few Ωm to 0.01 Ωm. **Fig. 2.7** presents a table from the work of Spagnoli et al. (2016) with 40 mini-core samples of massive sulphides, semi-massive sulphides with abundance of gangue minerals and host rocks. Listed are the bulk porosity, bulk density and the elctrical resistivity of each sample at 1 Hz. The difference in electrical resistivity between host rock and SMS deposits depends a lot on the metal and clay content, the connectivity of the sulphide grains and the porosities, but it is usually above 2 orders of magnitude.

No.	Sample name	Material	Bulk porosity	Bulk density (g/cm^3)	Electrical resistivity (Ωm)	Location of origin	Cu (wt.%)	Zn	Fe	Ba	Ca
1	MSM03/2-928DR-5	Basalt	0.080	2.96	124.40	Logatchev	–	–	–[a]	–	–[a]
2	MSM03/2-929DR-2	Basalt	0.016	2.87	70.27	Logatchev	–	–	–[a]	–	–[a]
3	MSM03/2-942DR-1	Gabbro-norite	0.017	3.00	17.79	Logatchev	–	–	–[a]	–	–[a]
4	MSM03/2-942DR-4	Gabbro-norite	0.012	2.93	85.91	Logatchev	–	–	–[a]	–	–[a]
5	MSM03/2-943DR-10	Basalt	0.075	2.94	48.79	Logatchev	–	–	–[a]	–	–[a]
6	SO109/3-69GTVA-3b	Altered basalt	0.046	2.94	60.40	Axial Smnt	–	–	–[a]	–	–[a]
7	SO157-15DS-1 FG	Basalt	0.275	2.76	31.06	PAR	–	–	–[a]	–	–[a]
8	SO157-17DS-4 FG	Basalt	0.079	2.98	23.87	PAR	–	–	–[a]	–	–[a]
9	SO157-18DS-5-FG	Basalt	0.102	3.07	18.92	PAR	–	–	–[a]	–	–[a]
10	SO157-38DS-Tubaf	Basalt	0.074	2.96	19.81	PAR	–	–	–[a]	–	–[a]
11	SO109/2-89GTV-M	Chimney (barite-rich)	0.166	3.65	4.42	Axial Smnt	<1	3	3	34	<0.1
12	SO109/2-89GTV-M (2)	Chimney (barite-rich)	0.176	3.63	6.96	Axial Smnt	<1	3	3	34	<0.1
13	EPR-South	Massive (silica-rich)	0.241	3.29	10.82	SEPR	<1	20	19	<0.1	<0.1
14	SO166-59GTVA-1B1	Chimney (Zn-Ba)	0.424	4.14	1.99	Pacmanus	<1	50	<1	9	<0.1
15	SO166-70GTVA-1C4	Massive (Zn-Ba)	0.334	3.79	1.70	Pacmanus	<1	50	2	9	<0.1
16	SO166-70GTVA-1G1	Massive (Zn-Ba)	0.233	3.93	4.68	Pacmanus	<1	55	3	4	<0.1
17	SO166-58GTVA-8A1	Massive (Zn)	0.315	4.16	16.13	Pacmanus	<1	53	2	5	<0.1
18	SO208-DR100-2A	Chimney (Zn)	0.302	3.16	3.31	Galapagos	<1	23	12	<0.1	<0.1
19	SO109/2-81GTVA-2(1)	Chimney (Cu-Zn)	0.360	3.87	0.49	Axial Smnt	12	10	12	<0.1	<0.1
20	SO109/2-81GTVA-2(2)	Chimney (Cu-Zn)	0.367	4.02	0.28	Axial Smnt	12	10	29	<0.1	<0.1
21	SO166-59GTVA-2A1	Chimney (Cu-Zn)	0.294	4.13	1.80	Pacmanus	8	23	6	<0.1	<0.1
22	SO166-58GTVA-6A	Massive (Cu-Zn)	0.405	3.78	0.07	Pacmanus	15	14	11	<0.1	<0.1
23	SO208-DR100-3A	Chimney (Cu)	0.434	3.90	0.11	Galapagos	12	5	29	<0.1	<0.1
24	ODM ROC-V557-324	Chimney (Cu)	0.115	3.94	0.06	Irinovskoe	26	1	25	<0.1	<0.1
25	ODM ROC-V557- 327	Chimney (Cu)	0.325	3.40	0.00	Irinovskoe	26	1	25	<0.1	<0.1
26	M64/1-114ROV-4E(1)	Chimney (Cu)	0.424	4.06	0.02	Turtle Pits	22	1	38	<0.1	<0.1
27	M64/1-114ROV-4E(2)	Chimney (Cu)	0.409	3.98	0.09	Turtle Pits	22	1	38	<0.1	<0.1
28	SO109/2-81GTV-4(1)	Chimney (Cu)	0.409	4.08	0.36	Axial Smnt	13	2	35	<0.1	<0.1
29	SO109/2-81GTV-4(2)	Chimney (Cu)	0.365	4.19	0.17	Axial Smnt	13	2	35	<0.1	<0.1
30	M64/1-124GTV-2E	Chimney (Fe)	0.402	4.23	0.19	Turtle Pits	6	3	37	<0.1	<0.1
31	M64/1-124-GTV-2I	Chimney (Fe)	0.381	4.61	0.11	Turtle Pits	6	3	37	<0.1	<0.1
32	M78/2-297ROV-1C	Chimney (Fe)	0.229	3.81	0.84	Turtle Pits	4	1	41	<0.1	<0.1
33	SO157-33GTV-Tubaf	Chimney (Fe)	0.279	3.31	0.79	PAR	2	2	34	<0.1	<0.1
34	EPR sulfide	Chimney (Fe)	0.026	2.90	0.70	SEPR	3	13	31	<0.1	<0.1
35	SO166-58GTVA-5G	Mineralized breccia	0.266	3.92	3.07	Pacmanus	8	6	5	8	2
36	SO166-70GTVA-2C1	Mineralized breccia	0.177	2.60	8.33	Pacmanus	<1	3	12	11	1
37	M64/1-139GTV-4A7(1)	Sulfate-rich breccias	0.215	2.62	2.69	Turtle Pits	2	<1	12	<0.1	14
38	M64/1-139GTV-4A7(2)	Sulfate-rich breccias	0.194	2.46	4.05	Turtle Pits	2	<1	12	<0.1	14
39	M64/1-139GTV-7A2(1)	Sulfate-rich breccias	0.128	2.96	2.09	Turtle Pits	6	<1	18	<0.1	10
40	M64/1-139GTV-7A2s	Sulfate-rich breccias	0.246	3.04	2.37	Turtle Pits	6	<1	18	<0.1	10

[a] Fe present but as silicate phase, not as conductive sulfide; Ca present but as silicate, not as sulfate

Figure 2.7: Table of physical properties, including electric resistivity for some SMS related minerals and surrounding rocks. Modified from Key et al. (2013).

2.2 The Marine Magnetotelluric Method

Magnetotelluric (MT) is a geophysical method that uses the earth's natural varying magnetic field to measure the resistivity of the earth. It is mainly set up by two different sources. The low frequency content, below 1 Hz, is set up by current systems in the magnetosphere generated from solar activity, **Fig. 2.8a**, and the high-frequency content, above 1 Hz, is generated from thunderstorms worldwide, see **Fig. 2.8b** (Johansen and Gabrielsen, 2015; Vozoff, 1991; Chave et al., 1991).

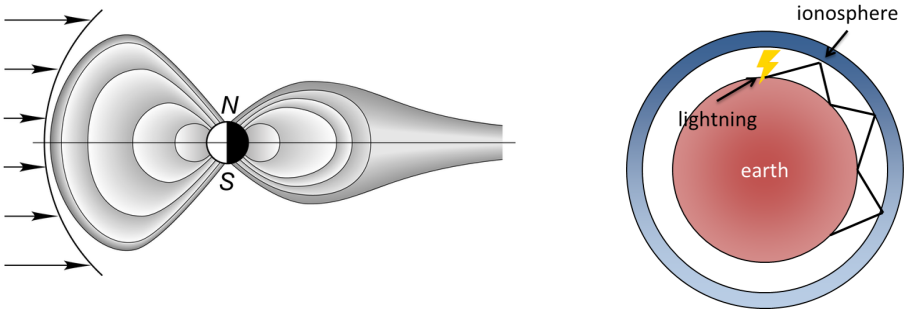

(a) Magentic field from solar winds contribute with frequencies below 1 Hz.

(b) Thunderstorms contribute with frequencies above 1 Hz

Figure 2.8: General principle sketch of MT. Modified from EM-GeoSci (05.06.17).

For both of the cases, the electromagnetic (EM) fields behave almost like plane waves that travel vertically downwards into the earth, see **Fig. 2.9**. Most of the waves are reflected back when it hits the surface of the earth, but part of the signal that penetrates the earth induces electrical currents known as telluric currents that will produce a secondary magnetic field (Naidu, 2012). The strength of the secondary field can be measured and depends on the electrical properties of the earth. This will contain information about the subsurface resistivity. In MT it is the low frequency signal set up by the solar wind-magnetosphere interaction that contributes the most. The conductive seawater will filter out most of the frequencies around 1 Hz and above. Being a signal created from the magnetosphere, the MT source signal will usually be stronger towards the poles and weaker around equator (Johansen and Gabrielsen, 2015).

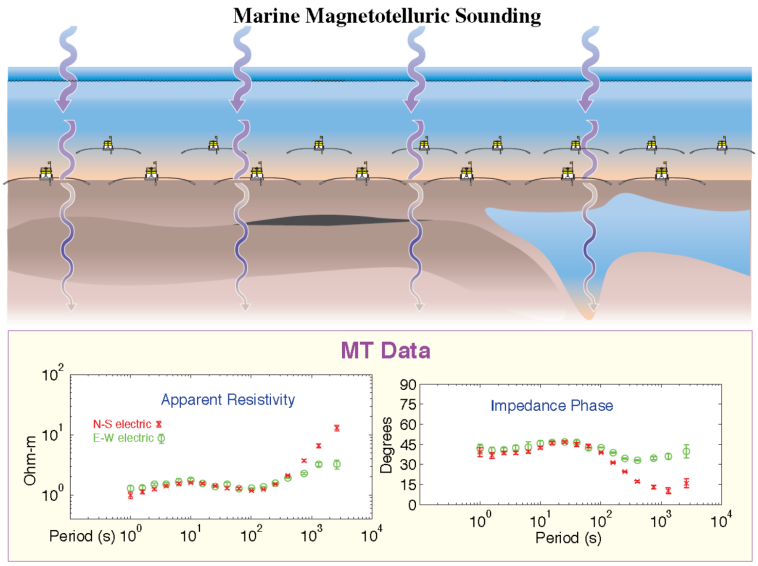

Figure 2.9: MT planar waves and receivers placed at the seabed. MT data of apparent resistivity and impedance phase (EMGS training material).

For acquisition of marine MT data, receivers are placed on the seabed like in **Fig. 2.9**. The same receivers illustrated in **Fig. 2.10** are used for both marine CSEM and marine MT acquisition, which often are done in combination.

The receivers are dropped from the survey vessel to the seafloor with a concrete anchor that is fitted with an acoustical release system (Zhdanov, 2009; Røsten et al., 2003). The receivers need to be highly sensitive, since the marine MT signal is extremely weak, and due to the low frequency signal, long listening time is advantageous. Typically, several days are needed to provide enough samples to describe the low frequency signal. Marine MT surveys in large water depths areas experience filtering of the high frequencies, which affects the imaging capabilities and leads to a loss of resolution in the shallowest parts of the section (Johansen and Gabrielsen, 2015). After the acquisition of the data, the concrete anchor is released by the acoustic system by a command from the vessel, and the receiver rises to sea level with help from the gas flotation sphere, see **Fig. 2.10** and is retrieved by the vessel (Zhdanov, 2009).

The recordings can be described by impedance tensors which can be found by looking at the relationship between the recorded E field (electric) and H field (magnetic):

$$Z = \frac{E}{H} = \frac{|E|e^{-i\varphi_E}}{|H|e^{-i\varphi_H}} = |Z|e^{-i\varphi_Z} \tag{2.4}$$

where Z is the impedance. $|E|$, $|H|$ and $|Z|$ are the magnitudes whilst $e^{-i\varphi_n}$ is the phase for n = E, H, or Z.

The processed data from the receivers are apparent resistivity and impedance phase like in **Fig. 2.9** as a function of the signal period (T). This is also the input for inversion of marine MT data. The two modes that are plotted is the transverse electrical mode (TE) and

the transverse magnetic mode (TM). TE is the electrical polarized mode where the electrical field is in the geological strike direction, as well as the TM is the magnetic polarized mode of the electrical field in the geological strike direction (Johansen and Gabrielsen, 2015). For a 1D earth, the apparent resistivity plot can be directly interpreted by looking at the separation of the two modes. From the apparent resistivity (ρ), an average of the subsurface resistivity is directly given, and from the signal period (T) it is possible to get an estimate of the minimum burial depth through the skin depth (δ):

$$\delta \approx 503\sqrt{\frac{1}{\sigma f}} \text{ or } \delta \approx 503\sqrt{\frac{\rho}{f}} \approx 503\sqrt{\rho T} \tag{2.5}$$

where σ is conductivity, f is the frequency, ρ is the resistivity and T is the signal period (Bhuyian et al., 2010).

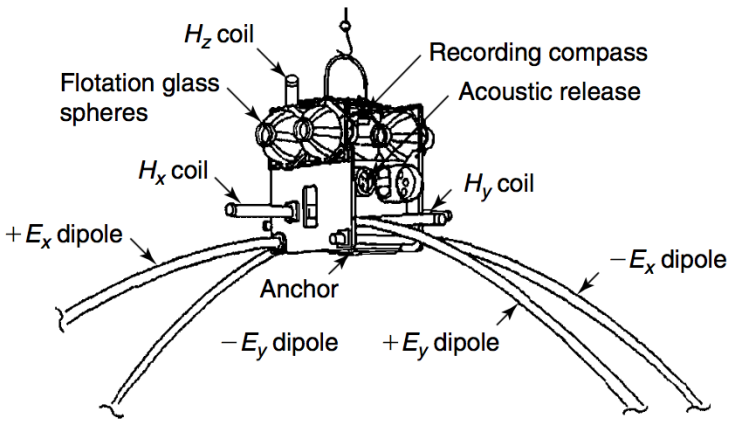

Figure 2.10: Marine MT and marine CSEM receiver. H_x, H_y and H_z coils measures the magnetic field components, whilst E_x and E_y dipoles measures the electric field components. Modified from (Zhdanov, 2009)

Key et al. (2013) shows that marine MT is well suited to image mantle upwelling at a mid-ocean ridge and Myer et al. (2013) shows how the method can be used to map conductive targets. Due to its low frequency content, marine MT can only image large-scale structures, but the EM fields can travel tens of kilometers into the subsurface (Johansen and Gabrielsen, 2015). Marine MT is, therefore, able to map conductive targets below high resistive strata such as basalt due to its sensitivity to subsurface conductors (Zhang et al., 1998). Zhang et al. (1998) has also proved that MT is useful for mineral exploration at depths where commercial EM is not logistically or cost competitive.

2.3 The Marine Controlled Source Electromagnetic Method

Marine controlled source electromagnetics (CSEM) uses a horizontal electric dipole (HED) source and an array of seafloor electric field receivers to transmit a low frequent electromagnetic signal in order to detect resistivity contrasts in the subsurface (Eidesmo et al., 2002; Johansen et al., 2005; Røsten et al., 2003; Bhuiyan et al., 2006). **Fig. 2.11** displays how the HED is towed above the receiver array at the seabed and emits low frequencies between 0.1 and 20 Hz (Johansen and Gabrielsen, 2015; Eidesmo et al., 2009). The receivers, which are the same as for marine MT displayed in **Fig. 2.10**, measure both the amplitude and the phase of the received signal that depend on the subsurface resistivity structures, see **Fig. 2.12** (Johansen et al., 2007). The rate of decay of the amplitude and phase shift are dependent on the subsurface geometry and by the attenuation represented by the skin depth as seen in equation (2.5) (Eidesmo et al., 2002). The EM fields have an exponentially decay by a factor of e^{-1} (Johansen et al., 2005; Constable and Srnka, 2007; Bhuyian et al., 2010). In general, the subsurface is more resistive than the seawater, and therefore, the signal is less attenuated and can propagate into the subsurface.

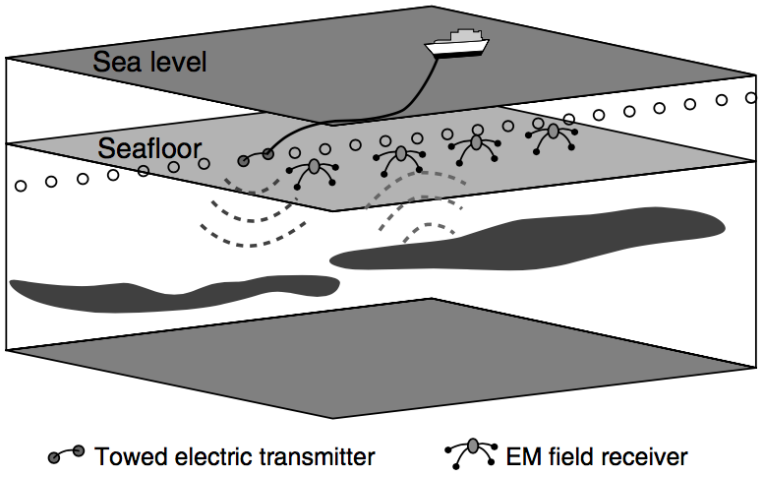

Figure 2.11: Cartoon of how CSEM is aquired on the seabed. A general survey configuration where an electric transmitter is towed by the survey vessel above receivers that record the EM response from the geoelectrical structures beneath the seafloor. Modified from Zhdanov (2009).

An important part of CSEM is the sensitivity study that is done prior to the acquisition (Bhuyian et al., 2010). The expected response from a resistive or conductive target is calculated and analyzed by forward modelling. Several factors of the targets are taken into account, such as geometry, resistivity, burial depth and contrast of surrounding rocks. **Fig. 2.12** shows an easy illustration of how it is possible to calculate sensitivity. The two top curves are the phase shift where the red is from the target response while the blue is the background response. The two curves in the middle are the magnitudes, again, red is the target response, and blue is the background response. The green curve is the absolute

field difference of magnitude and phase and represents a scattered field response from the target. The purple curve is the assumed data uncertainty and noise. The data is sensitive to the target when the scattered field is above the uncertainty of the data (grey area) (Johansen and Gabrielsen, 2015).

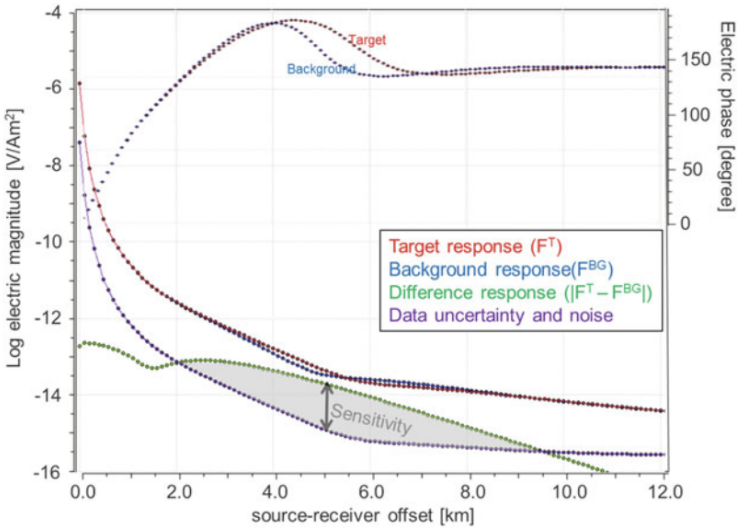

Figure 2.12: Illustration of how sensitivity to a resistive layer can be calculated. Magnitude and phase curves for a target (red curve) and a background (blue curve) are plotted versus source-receiver offset. The scattered field (green) is the difference between the target and the background for phase and magnitude. Sensitivity to the target is found if the scattered field response is above the expected data uncertainty and noise (purple curve). Modified from Johansen and Gabrielsen (2015).

When acquiring marine CSEM data the receivers are placed in a grid for 3D (if 2D it is along one receiver line) at the seafloor covering the area of interest. The receivers are illustrated in **Fig. 2.10**. **Fig. 2.11** show how a 2D case with only one receiver line will look like. A vessel tows the HED source above the receivers (usually a few tens of meters) and the HED excites a low frequency EM signal that diffuses horizontal and vertical current flow (Um and Alumbaugh, 2007; Constable and Srnka, 2007) outwards both in the overlying water column and downwards into the seabed (Eidesmo et al., 2002; Røsten et al., 2003), like in **Fig. 2.13**.

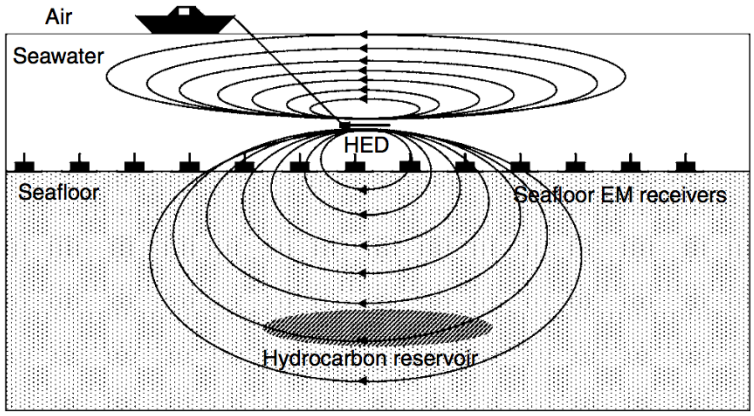

Figure 2.13: Marine CSEM concept diagram of a vessel towing the HED above seabed receivers. Contour lines represent electrical current flows. Modified from Um and Alumbaugh (2007).

The receivers register a combination of the different signal pathways such as the transmission directly trough seawater, reflection, and refraction through the seawater-air interface, reflection and refraction along the seabed and reflection and refraction trough any high resistive subsurface layers (Johansen et al., 2007; Bhuiyan et al., 2006; Johansen and Gabrielsen, 2015). In all of the different pathways, the signal will be attenuated at different rates. **Fig. 2.14** shows the different paths or modes that the current can propagate along. The blue arrow is the direct wave that arrives the receivers directly from the HED source. High attenuation on the seawater will damp this response, but it will still be dominant for short offsets (Johansen et al., 2005, 2007; Bhuiyan et al., 2006). The green arrows are diving waves that propagate through the seabed and takes with them information about the subsurface and how much they have been attenuated. The purple arrows illustrate the refracted waves that due to a resistive layer under a critical angle sets up guided waves that leak information back to the receivers (Eidesmo et al., 2002, 2009). At intermediate offsets, between 2000 m and 8000 m at **Fig. 2.15** the subsurface waves will dominate (Johansen et al., 2007).

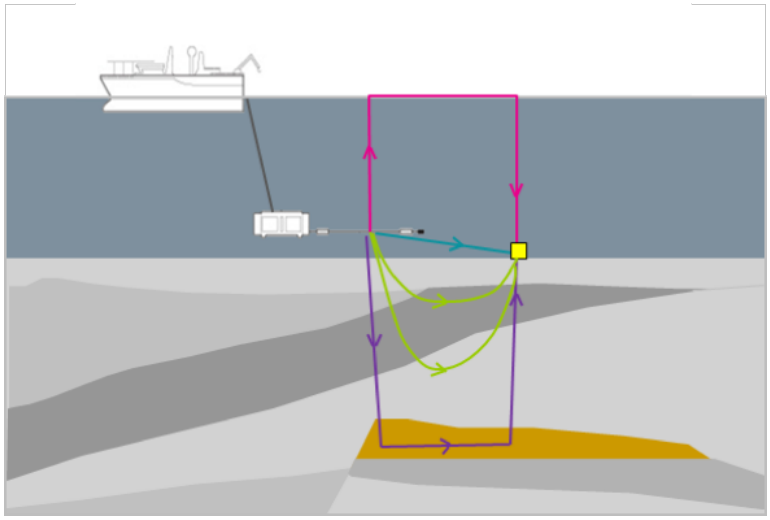

Figure 2.14: The different modes that occurs in marine CSEM. Pink arrows: air wave, blue arrow: direct wave, purple arrow: refracted wave and green arrows: refelcted waves (EMGS training material).

The pink arrow is what is known as the air-wave. It diffuses upward from the HED source to the air-water interface and propagates along this interface with only laterally geometric spreading loss before it diffuses back down to a receiver (Um and Alumbaugh, 2007). This effect will be dominant for large offsets, but it is dependent on water depth (Johansen et al., 2007; Bhuiyan et al., 2006). Shallow water column provides less conductive material to diffuse through to attenuate the signal, compared to deep water depth where the large water column will attenuate most of the air-wave effect. Hence, in shallow waters, the air-wave effect will arrive at shorter offsets than for large water depths. **Fig. 2.15** shows electric field amplitude and phase for a conductive subsurface (grey line) and a more resistive subsurface (yellow line). The top plot is magnitude versus offset (MvO) and is a measure of the received field strength, while the lower plot is phase versus offset (PvO) where the phase shift is a measure of how much of the received signal is delayed with respect to the source signal. For the MvO plot, there is not much difference in the responses smaller than 2000 m offset. After that, a high resistivity anomaly can be seen as there is less attenuation of the magnitude than there is for the background signal. The ”bend” on the background magnitude is due to the air-wave. This can not be seen on the yellow line as the signal from the subsurface resistor is still strong enough to dominate. For the phase shift plot, there is also a separation around 2000 m offset. Steep phase curve means that the phase velocity is low and the travel time is long leading to a large phase shift. In the resistor (yellow curve), the phase velocity is higher and therefore the curve flattens out as the travel time is short and the phase shift is small (Eidesmo et al., 2009). The ”bend” on the background phase curve is a ”roll-over” effect caused by the air-wave which also flattens the curve out almost completely when it dominates the data (Um and Alumbaugh, 2007).

Kowalczyk et al. (2015); Imamura et al. (2011, 2012) show that buried SMS deposits

can be mapped using marine CSEM methods. Marine CSEM can also be used to determine the burial depth of the deposit, together with its extent (Kowalczyk et al., 2015).

It is easy through sensitivity studies to show that CSEM is sensitive to a given target or structure. However, a measurable anomaly does not mean that one is able to reconstruct a resistivity model from the data. Due to non-linearity and non-uniqueness of the problem, it is difficult to use the theoretical techniques for assessing the resolution (Key, 2012a). It is therefore strongly recommended to perform a synthetic forward modelling and inversion study. This will be further discussed in the following chapter and in the discussion.

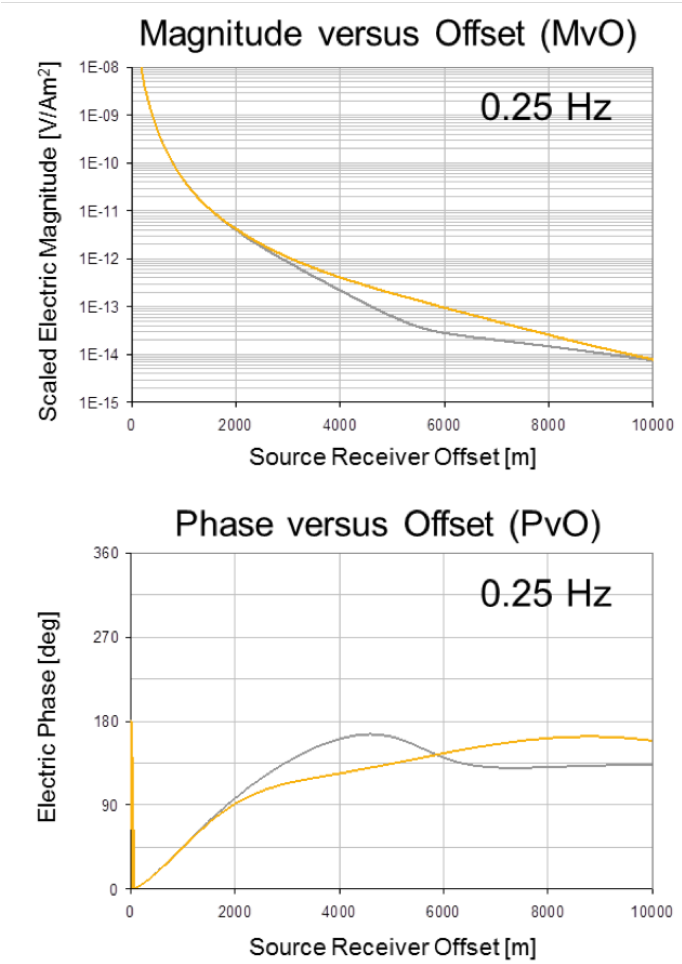

Figure 2.15: Magnitude versus offset and phase shift versus offset. The MvO has been ”scaled” by the source dipole moment (source current x source length) and hence has units [V/Am2] instead of [V/m]. Yellow curves are the resistive target response whilst the grey curve is the background model response. Less attenuation for higher resistivity target leads to higher magnitude and lower phase angle (EMGS training material).

2.4 Forward modelling and Inversion of EM Data

2.4.1 Forward modelling

Before a marine MT or marine CSEM survey is carried out, it is normal to do a feasibility study. Parts of the study will be modelling and inversion of synthetic data in order to try to replicate the real survey that is going to take place. Typical goals of the forward modelling are to establish optimal survey locations and receiver geometry, but it is also useful to quantify the expected electromagnetic response from the targets (Johansen et al., 2005; Johansen and Gabrielsen, 2015). It is also a playground, where all types of different values and properties could be tested, in order to get a better understanding of the actual received data after acquisition.

In a feasibility study, the model space is where the initial resistivity model is built. Then, forward modeling is done in order to generate synthetic data or modeled data.

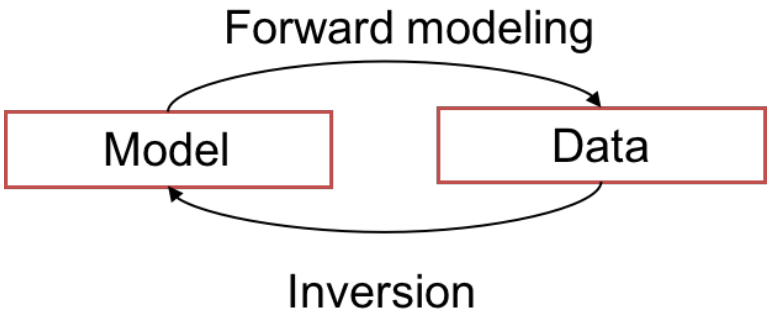

Figure 2.16: Relations between data and model (EMGS training material).

From equation (2.6) it is shown that each model has one specific response. The data (d) represents one specific response from the resistivity model (R), whilst G is a forward operator that reflects the physics behind Maxwell's equations solved by a computer.

$$d = G(R) \tag{2.6}$$

The forward problem is always well-posed. Given a certain earth model, it is certain that there is a single, unique solution that describes the EM field behavior (Zhdanov, 2009). A well-posed problem means also that in addition to there being a solution that also is unique (same data can only be described by one model), it is also stable, which means that a small change in the model would lead to a small change in the data measurements. Should one or more of these criteria be broken, it is an ill-posed problem (Johansen and Gabrielsen, 2015).

2.4.2 Inversion

Inversion is the process where one goes from synthetic or observed data to a resistivity model. From **Fig. 2.16** it is illustrated as the opposite process from forward modelling, as the goal now is to replicate a subsurface resistivity model from given data.

Fig. 2.17 illustrates how the inversion algorithm works. First, an initial model R_0 is made from a qualified guess of a resistivity model. During the forward modelling of the start model, source and receiver geometry like for a real data case is added. Then, the forward modelled data is compared to the survey data and the misfit between them are calculated. This is also called cost function, and the goal of the inversion is to minimize it. If the misfit is unacceptable, the model is updated, R_{n+1}, and a new loop is started. A new round of forward modelling will be executed on the synthetic data and again it will be compared to the survey data. One finished loop is called an iteration, and this inversion loop is repeated until the difference between the synthetic data and the input (survey) data is in the order of the data uncertainty (Johansen and Gabrielsen, 2015).

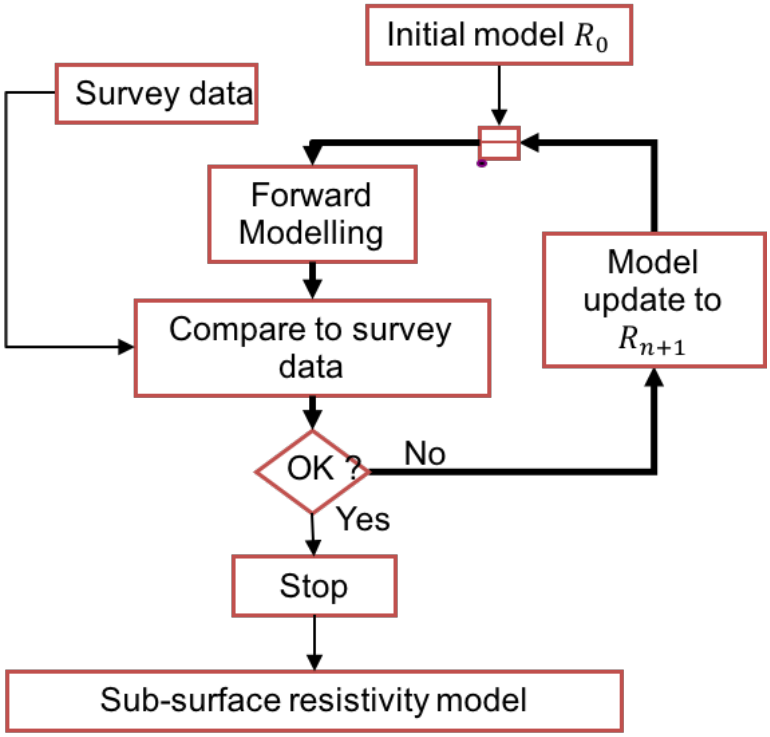

Figure 2.17: Inversion loop (EMGS training material).

There is no inverse operator for G that can be solved, therefore an iterative approach is used for the model update:

$$R_{n+1} = R_n + \Delta R \tag{2.7}$$

which is achieved by minimizing an objective function:

$$\varepsilon = \varepsilon_{data} + \varepsilon_{reg} \tag{2.8}$$

where ε_{reg} is the regularization term and ε_{data} is the data misfit and is defined as:

$$\varepsilon_{data} = \Sigma W^2 \frac{|E^{obs} - E^{synth}|^2}{(\delta E)^2} \tag{2.9}$$

where W is a data weight which depends on offset and uncertainty for each data sample, and δ is the data uncertainty. $E^{obs} - E^{synth}$ is the difference between the observed electrical field data and the synthetic electrical field data (Tikhonov and Arsenin, 1977; Tarantola and Valette, 1982). The data misfit is summed up for every receiver, transmitter, and frequency.

An inversion problem is an ill-posed problem. It has no unique solution, which means that there are several resistivity models that can create the same data. A small change in the data leads to a large change in the model. This is also one of the largest challenges with marine MT and marine CSEM and is called non-uniqueness.

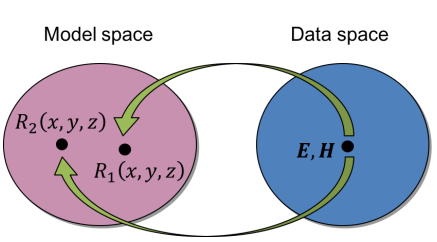

(a) One set of data may give different models, R_1 or R_2 in this case.

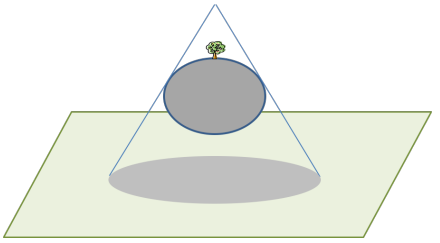

(b) Illustration of what non-uniqueness looks like.

Figure 2.18: Illustrations of non-uniqueness (EMGS training material).

Non-uniqueness can be illustrated by **Fig. 2.18** where in **Fig. 2.18a**, the observed data (d), are represented by the electric field E and magnetic field H. Both models R_1 and model R_2 in the model space are possible solutions to the given data. It is an undetermined problem due to insufficient data, and that the data are noisy and uncertain. An analog for non-uniqueness can also be described from **Fig. 2.18b**. It is like to try to determine the shape of an object based on its shadow.

One way to narrow down possible models that fit the data are through regularization terms. A regularization function $\varepsilon_{Reg}(R)$ should be chosen such that models with desirable properties are assigned low values, **Fig. 2.19a** (Zhdanov, 2009). Regularization can be based on a smoothness requirement, sharp contrast requirement, consistence with structure from seismic or with a priori resistivity information. **Fig. 2.19b** shows how the R_1 model is more desirable based on the low value of $\varepsilon_{Reg}(R)$ in **Fig. 2.19a**.

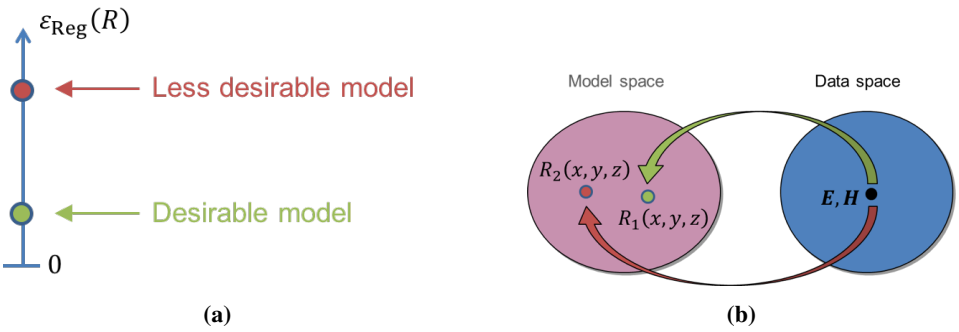

Figure 2.19: Regularization favours certain types of models (EMGS training material).

It is also possible to put constraints on the inversion in form of other geophysical or geological data, which will limit the number of solutions and force the inversion to go in one direction (Johansen and Gabrielsen, 2015). Also, it is important to carefully build the start model for the inversion. It should be close to a global minimum on the misfit function, **Fig. 2.20**. If the start model is too far from the true model the inversion may converge towards a local minimum instead of the global.

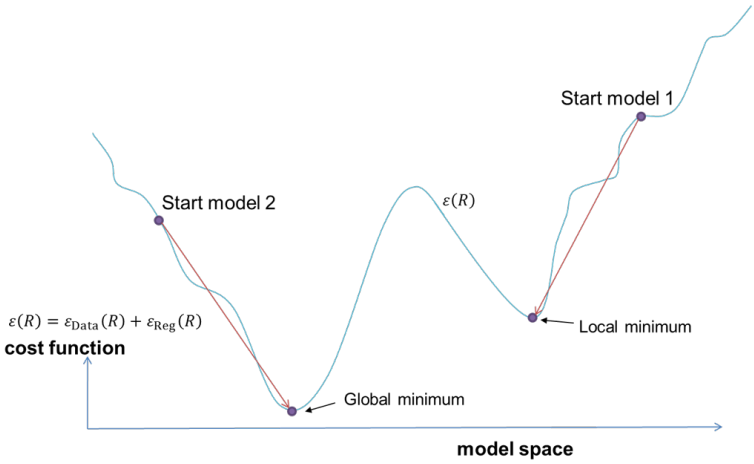

Figure 2.20: Example for a misfit function fot a one-dimensional inverse problem (EMGS training material).

For the inversions done in this thesis, the forward problem is solved by a parallel adaptive finite element method implemented using unstructured triangular finite elements that conform to the inversion parameters. The inversion algorithm is the same as explained in this chapter, but the mathematics behind it is discussed in Key (2012b).

Chapter 3

Methods

In this section, the foundation of how the results were generated and the process of how it was achieved will be discussed. From the geometry used from the interpretation of seismic sections, through model-building, modelling of synthetic data and finally how the inversion results were performed.

In the process of achieving the results, several types of software have been used; MATLAB, PETREL, and MARE2DEM. PETREL is widely known and for this thesis the use of PETREL has been limited to some interpretation and extraction of horizons, and nothing that needs any further explanation. MATLAB is also a known software and is used as a front-end and back-end to MARE2DEM, but MATLAB itself will not be discussed, but rather how it was used together with MARE2DEM in this case.

3.1 Theoretical workflow of the study

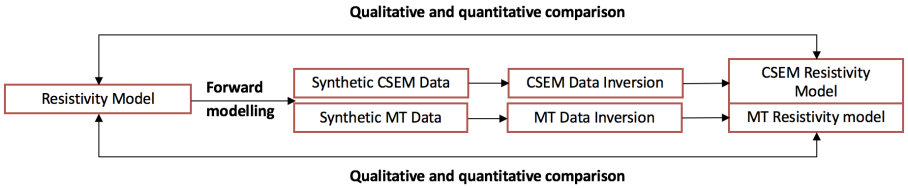

Figure 3.1: Workflow used in the study.

The goal of this study is to investigate if it is possible to detect and image SMS deposits with marine CSEM and image the asthenosphere with marine MT and marine CSEM. To achieve the goals, several steps have been followed over and over again. The workflow is illustrated in **Fig. 3.1** and starts with a resistivity model that through forward modelling generates synthetic data for the specified method, which is either CSEM or MT. The next step is an inversion of the synthetic data, where the loop in **Fig. 2.17** is followed until

the misfit is accepted. That produces and inversion resistivity model which then is compared with the forward start model from the initial step. For a low misfit value, a close resemblance with the forward start model should be seen in the inverted resistivity model.

Fig. 3.2 illustrates how a synthetic resistivity model could look after it has been built. **Fig. 3.3** shows the unstructured grids applied to the inversion model that has a goal to replicate **Fig. 3.2** as good as possible based on the synthetic data, and also the results after CSEM inversion (middle) and joint MT and CSEM inversion (bottom).

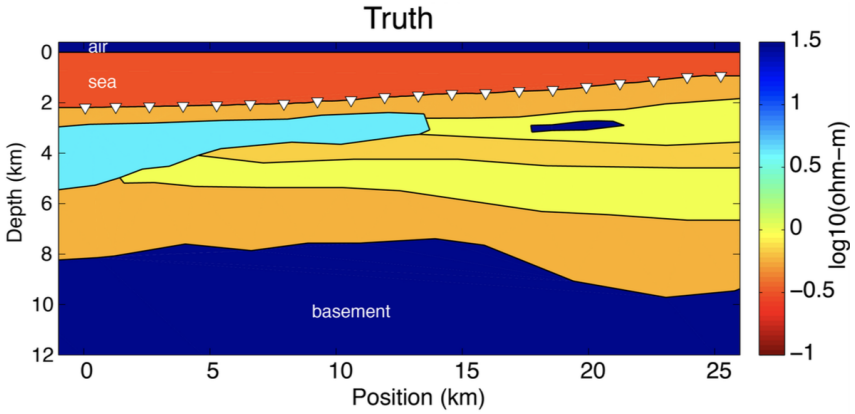

Figure 3.2: Illustration of synthetic model. (Key, 2012b)

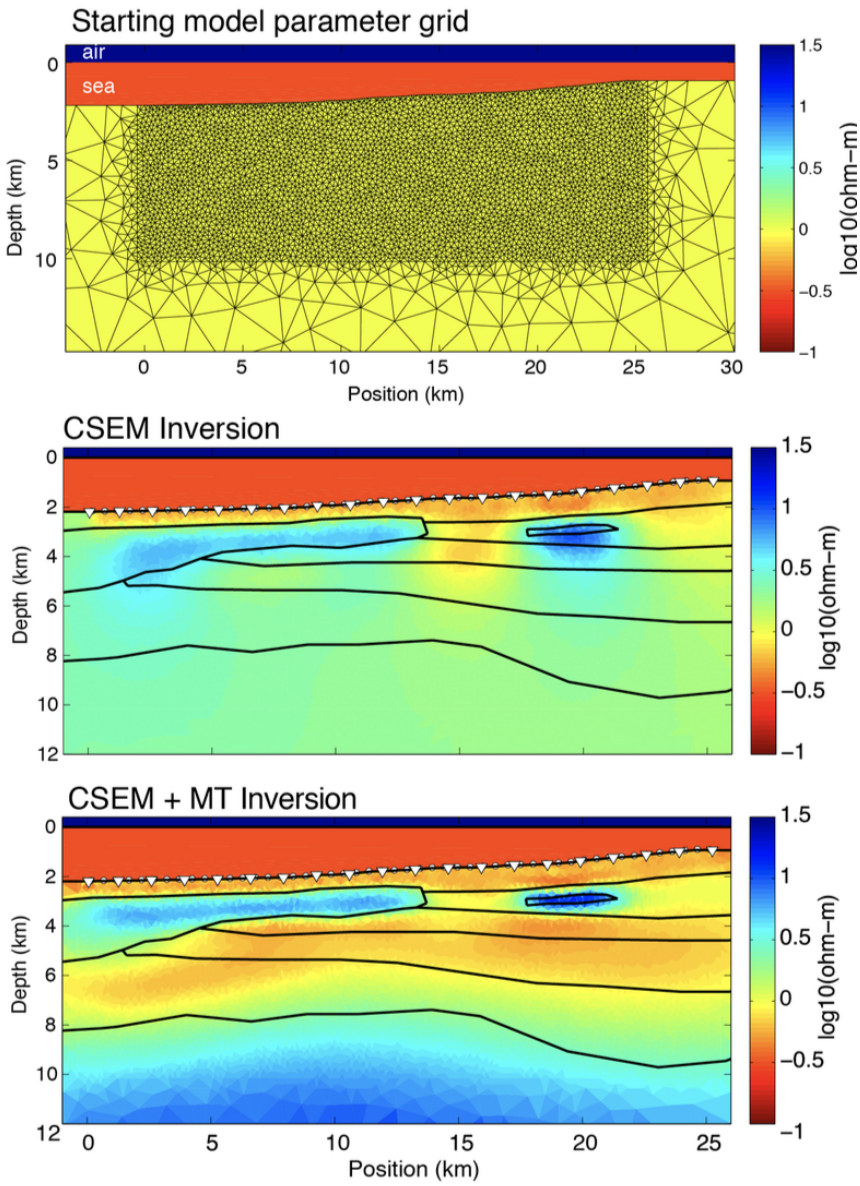

Figure 3.3: Illustration of the process from inversion start model to final inversion resistivity model (Key, 2012b).

3.2 MARE2DEM Content and workflow

MARE2DEM is an open source software. It is not streamlined but works great for academic use and research. It includes MATLAB programs scripts for visualization of the data and for building the forward model and the inversion model. The workflow for MARE2DEM is illustrated in **Fig. 3.4**. The different processes within the workflow will be highlighted below, but the main part is that MARE2DEM uses MATLAB as a front-end model building tool as well as a back-end plotting and imaging tool for results and data. Geological structures or horizons can be imported into the model builder Mamba2D in order to create the model. After the resistivity model is created, it is forwarded into MARE2DEM for forward or inverse modelling. The results are then imported back into MATLAB for quality control and viewing of results.

Mamba2D is the model builder assistant that is used to create the forward model and the start model for inversion. Also, scripts are available for creating the forward CSEM and MT data files. Several files are used as input into MARE2DEM. The data files specify the sources, receivers, and frequencies as well as the type of data to be modelled. The model file specifies the geometry of the model parameter grid, while a penalty file contains the inversion's roughness penalty matrix used for regularization. All of these files are listed by the resistivity file created in Mamba2D, which is first read by MARE2DEM. It includes the resistivity of each model region, if there is any anisotropy, inversion model bounds and prejudices (MARE2DEM, 06.06.17).

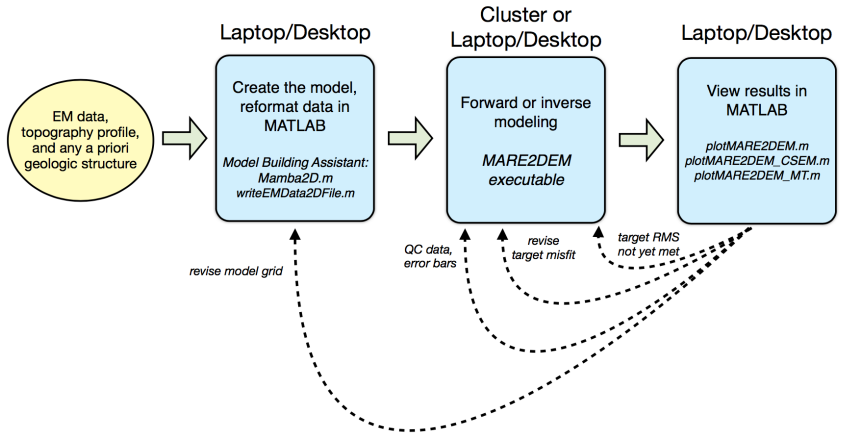

Figure 3.4: The workflow of MARE2DEM. Modified from MARE2DEM Tutorial and Training (MARE2DEM, 06.06.17)

3.3 MARE2DEM walkthrough

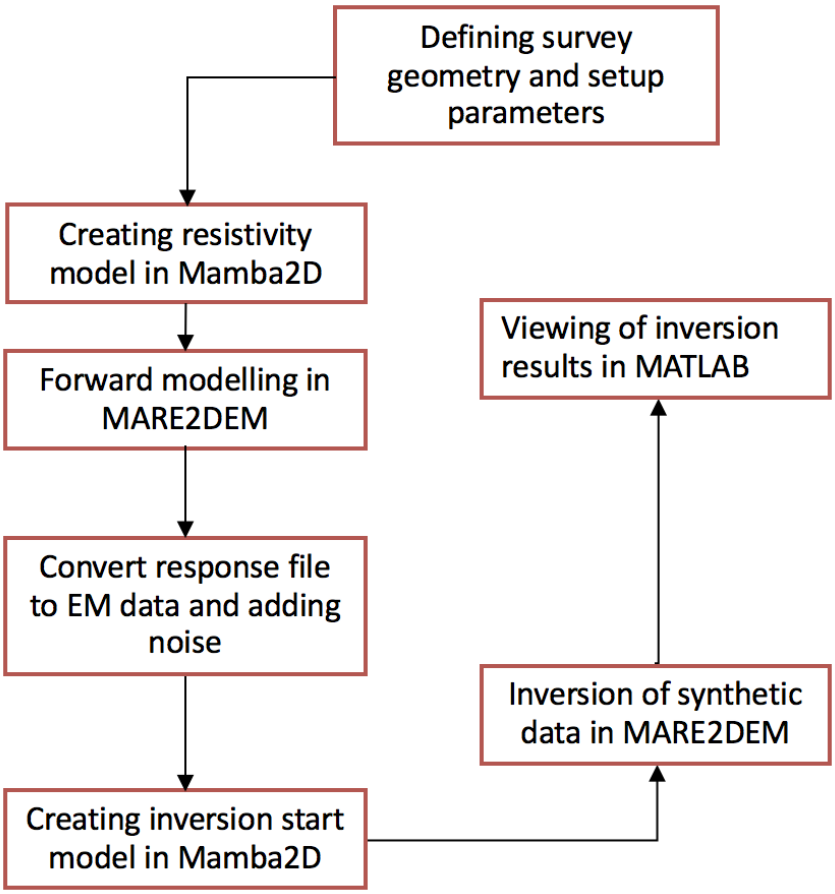

Figure 3.5: Workflow of the method

In this section, the fundamentals of how the results were generated are represented. The workflow is described below and is illustrated in **Fig. 3.5**.

In order to create a model, some geometry from the specialization project was used. The seismic sections were interpreted in PETREL and those that have been used in the master thesis were reviewed and interpreted with a higher focus on sediment packages than before. Interpreted seismic horizons of the seabed, the top basement, and some sediment interfaces were taken from PETREL and imported for use in MARE2DEM.

MARE2DEM is a parallel adaptive finite element code for 2D forward and inverse modelling of electromagnetic geophysical data. It uses MATLAB as a front and rear-end plotting software, and it is also in MATLAB through the model builder assistant Mamba2D, that the different models for forward modelling and inversion are made.

MARE2EM itself runs in this case on a cluster with enough cores to deal with the inversion. The program itself doesn't have a graphical interface. It is a command line code for running the forward modelling and the inversion.

Initially, the geometry of the receiver positions needs to be determined and for seafloor receivers, it is convenient to place the receivers slightly above the seafloor so that MARE2DEM uses the seawater conductivity rather than the seafloor when converting currents to electrical fields. As in a real survey where the electrical field sensors are located in the seawater above the seafloor, a shift of 0.1 m above the seafloor is sufficient.

The seismic horizons taken from PETREL was interpreted in two-way traveltime, but for the model building, it is necessary to convert them into depth. The Mamba2D model builder in MATLAB has an easy interface the geometry and the parametrization of the resistivity model can be defined. As seen in **Fig. 3.6**, there is a lot of ways to build a model in Mamba2D. Either from scratch where one can draw the model by hand, or by importing segments from seismic interpretation as is done in this case, together with a handmade geometry of the magma chamber and deeper parts the model. The final forward model can be seen in **Fig. 3.7**

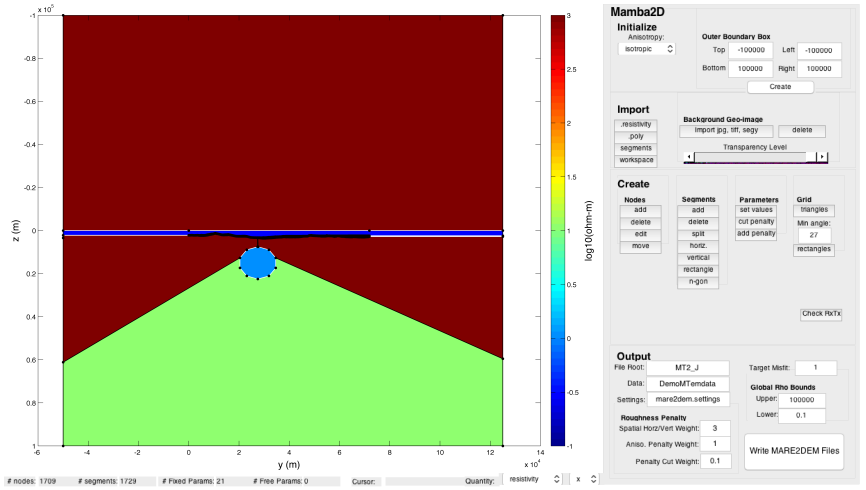

Figure 3.6: The interface of the assistant model builder in MATLAB: Mamba2D with a large scale model.

Each part of the model is then given a resistivity value that suits its geological properties, and this is stored together with the geometry in a model file that is, together with a file defining the survey parameters, sent to MARE2DEM for forward modelling. The forward code in MARE2DEM then generates synthetic data. In the next step, noise is added to the synthetic data and stored in a different file format.

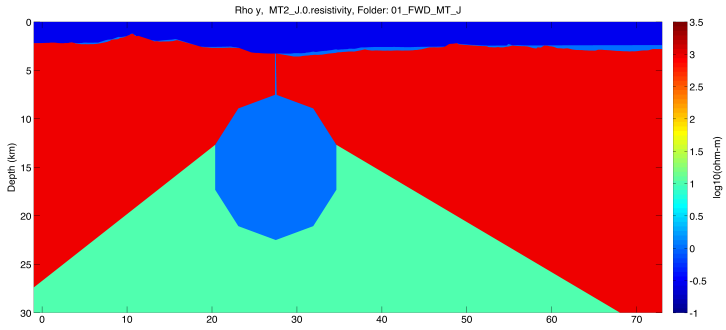

Figure 3.7: Model used for the large scale regional study.

As the forward resistivity model, the start model for inversion is built with the help of Mamba2D, while using the same geometry for the seabed, this model is very simplified, as it is just an initial guess of how the model could possibly look like. It is created as a halfspace with the sea surface and the seabed as the only restricted surfaces. This study want's to test the capability of CSEM and MT to reconstruct the subsurface resistivity structure, therefore only a simple halfspace is used as start model. Resistivity values for air and seawater are fixed.

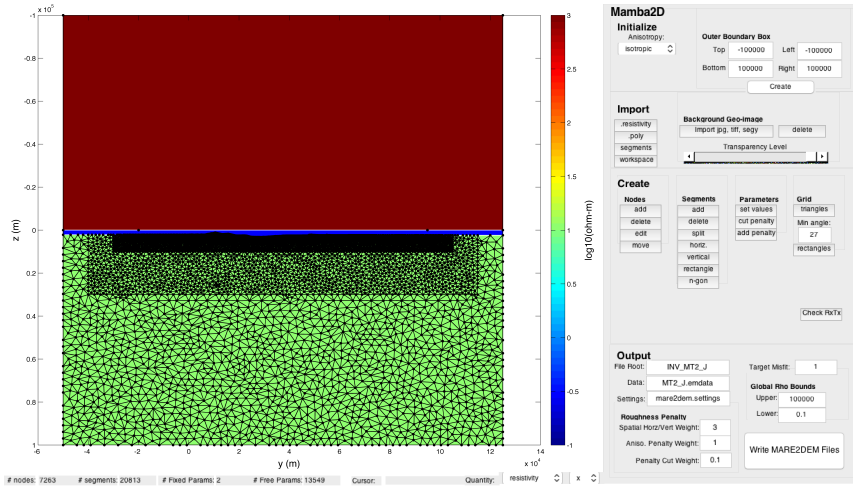

Figure 3.8: Inversion start model with air (dark red), seawater (blue), and subsurface(green). The black lines are the gridding patterns that are selected for each region.

The inversion model is discretized using triangles and rectangles with varying size. They are small below the seafloor and increase with depth as the resolution of EM decreases, see **Fig. 3.8**.

MARE2DEM performs an OCCAM type of inversion, where the aim is to find the smoothest possible model that explains the data.

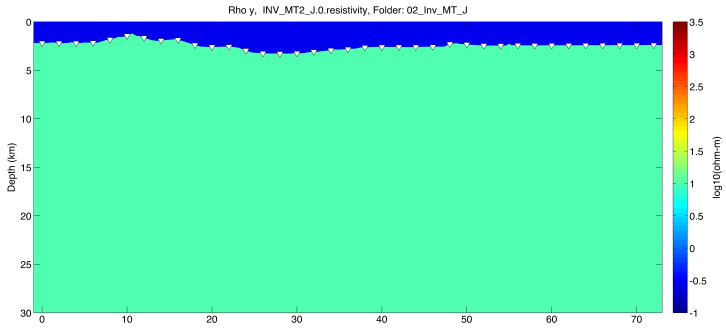

Figure 3.9: Inversion halfspace; the initial resistivity model that is inserted into MARE2DEM for forward inversion modelling. On a logarithmic scale, with a resistivity of 10 ohm-m for the subsurface, while seawater has fixed resistivity of 0.3 ohm-m.

MARE2DEM updates the resistivity model by itself and after each iteration it gives a response file containing synthetic data and a new resistivity file containing the updated model. Then, most of the cells in the halfspace have then been altered and updated with the new resistivity value and the inversion continues iterating goes on to try to minimize the misfit. After the iteration process should reach a misfit close to 1, which means the model fits the data within the desired data uncertainty. The results are imported back into MATLAB for plotting and viewing of results.

During the inversion, the goal is to get as close as possible to the initial starting model as possible, **Fig. 3.7**. One result could be something like in **Fig. 3.10**

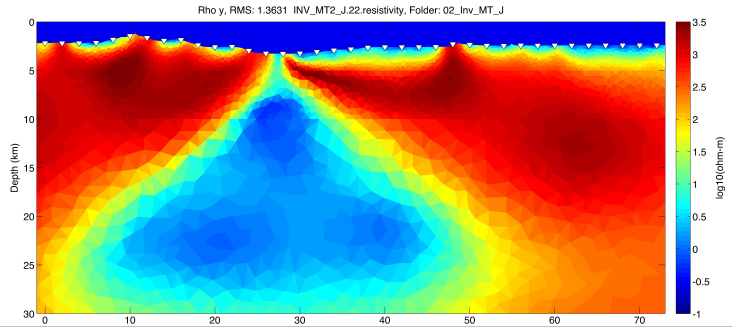

Figure 3.10: Final iteration with a RMS misfit of 1.3631 after 22 iterations. The result is after an MT inversion of MT generated data.

3.4 Background data

Like discussed above, the geometry of the seafloor and the top basement is from a seismic section from the Mohn-Knipovich Ridge between Jan Mayen and Svalbard. They were interpreted in the specialization project last semester and now used to create the framework for the electromagnetic resistivity models, see **Fig. A.1** for the location of the CSEM modelling and inversion of SMS deposits from the seismic. Other geometries in the models, such as the magma chamber in **Fig. 4.3a** are influenced by Key et al. (2013), where also the resistivity values are taken from. This geometry also fits well with the Conley and Dunn (2011) version of the mantle structure at the ridge, **Fig. A.2** in the appendix, and the values with the table of resistivity values from Spagnoli et al. (2016) seen in **Fig. 2.7**.

No.	**Geometry**	**Resistivity** (Ωm)
1	Air	1×10^{13}
2	Seawater	0.3
3	Sediments	1
4	Basement	1000
5	Magma chamber	1
6	Deep partial melt	10
7	SMS	0.2

Table 3.1: Resistivity values used in the forward models - Chosen from resistivity values given in Key et al. (2013) and Spagnoli et al. (2016)

Table. 3.1 displays the resistivity parameters that were used in the forward start model, whilst **Table. 3.2** displays the resistivity parameters used in the inversion start model for this project.

No.	**Geometry**	**Resistivity** (Ωm)
1	Air	1×10^{13}
2	Seawater	0.3
3	Halfspace	10

Table 3.2: Resistivity values used in the inversion start model.

Chapter 4

Results

In this chapter, the results from the 2D synthetic forward modelling and inversion study will be presented. How the geometry of the sections was chosen, how the electric properties were chosen will be clarified and the different variations of parameters that have been used to produce each result will be presented. The workflow that is used to provide the results can be seen in **Fig. 3.5**.

In the forward modelling and inversion study that were carried out, this is the different tests that were done and that will be presented:

- Large scale imaging of the asthenosphere with a magma chamber

  Using marine MT and marine CSEM

- Size dependent imaging of SMS with marine CSEM

  Large SMS deposits (used as reference case through the rest of the study)

  Small SMS deposits

- Frequency dependent imaging of SMS deposits with marine CSEM. Compared to all frequency case

  Low frequencies [0.25 Hz, 0.5 Hz, 1.0 Hz, 2.0 Hz]

  High frequencies [4.0 Hz, 8.0 Hz, 16.0 Hz, 32.0 Hz]

- Receiver spacing dependent imaging. Compared to 1 km case

  2 km receiver spacing

  750 m receiver spacing

where the ”Large SMS deposits” case is used as a reference case for the following tests, with 1 km receiver spacing and all frequencies included.

4.1 Data Sensitivity to Astenosphere

From the forward modelled data, consider a background halfspace (blue curve) of high resistivity basement, **Fig. 4.1a** (1000 Ωm) compared to a model with a deeper conductive zone (red dashed curve) like **Fig. 4.1b**. The conductive zone will give a lower apparent resistivity, top both figures in **Fig. 4.2** and a decrease in phase, which is higher phase degree values, bottom figures. The data are from receiver 033 at receiver position 64 km with all MT frequencies and **Fig. 4.2a** shows the TE mode whilst **Fig. 4.2b** shows the TM mode for the same receiver.

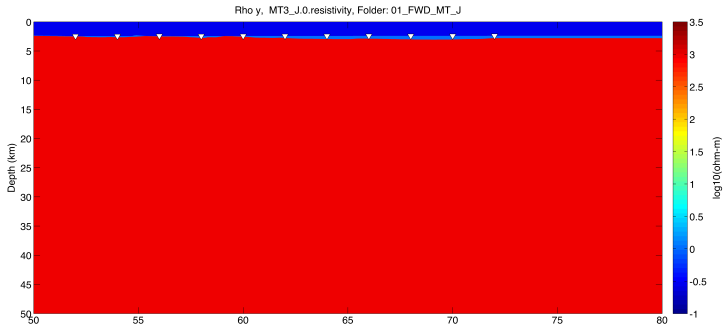

(a) MT background model. Resistive basement of 1000 Ωm.

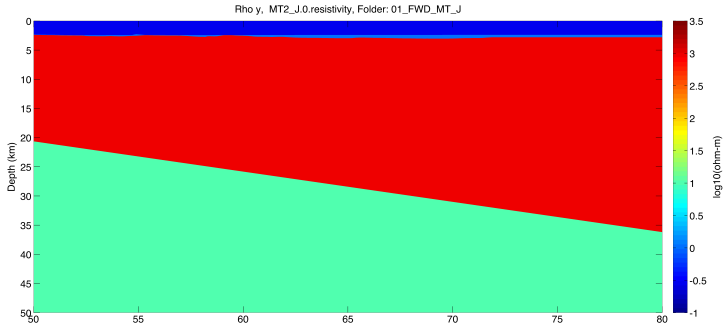

(b) MT model with less resistive features. Outcrop of model in **Fig. 4.3a**

Figure 4.1: Background model (a) and model with less resistive features (b).

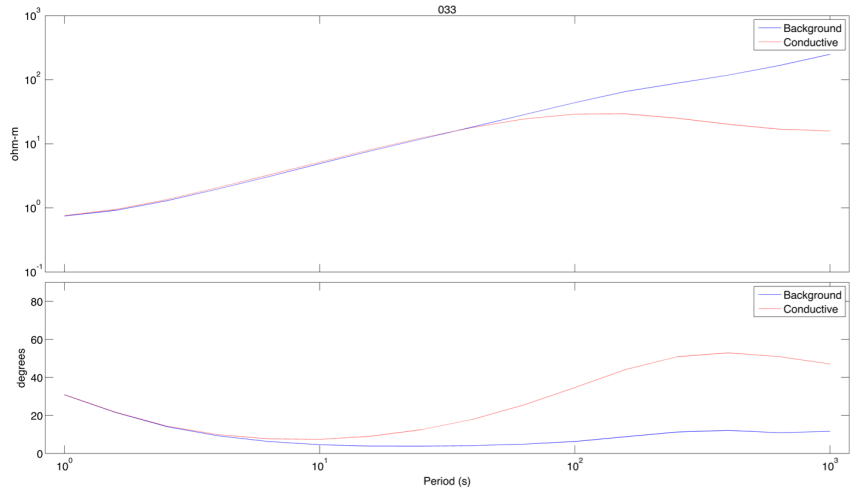

(a) TE mode. Apparent resistivity at the top and impedance phase at the bottom. Blue curve represents the background model and red curve the more conductive model.

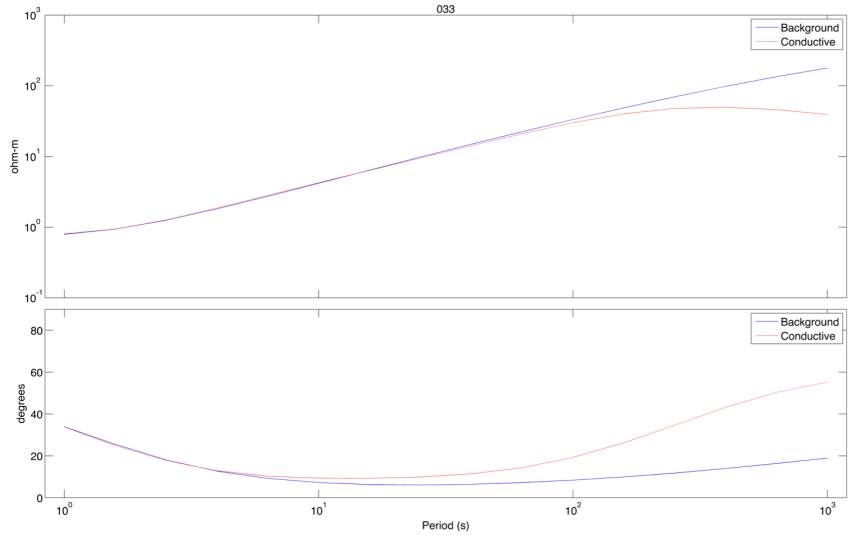

(b) TM mode. Apparent resistivity at the top and impedance phase at the bottom. Blue curve represents the background model and red curve the more conductive model.

Figure 4.2: TE and TM modes for background model and a more conductive subsurface model.

4.2 Imaging of a Magma Chamber and the Astenosphere

In **Fig. 4.3** the objective was to image a magma chamber below the mid-ocean ridge, much like what was done in Key et al. (2013), but through MT modelling and inversion. The same structure as in Key et al. (2013) was used, but with different dimensions. A conceptual model was chosen in order to ease the imaging. Sixteen frequencies between 0.001 Hz and 1 Hz was used and receivers were placed every 2 km along the whole section (0-72km) making up a total of 37 receivers. In **Fig. 4.3a** the top blue area represents the seawater (10 Ωm), the next lighter blue layer represents the sediments (1 Ωm) and the red area is the basement (1000 Ωm). The blue area in the middle is the magma chamber with a feeder (1 Ωm) that goes all the way to the seafloor, and the green area is the deep partial melt (10 Ωm) below the magma chamber. **Fig. 4.3b** colours show log[resistivity (Ωm)] in the vertical directions obtained by MT inversion after 22 iterations with a misfit of 1.3631. The horizontal scale is in km away from the zero point to the west on the line.

In **Fig. 4.3c** the same initial model, **Fig. 4.3a**, was used, but CSEM forward modelling and inversion was executed instead of MT. 2 km spacing between the receiver were also used in this case, and four frequencies (0.25 Hz, 0.5 Hz, 1.0 Hz and 1.5 Hz) was chosen. After 25 iterations, the misfit ended at 1.0897.

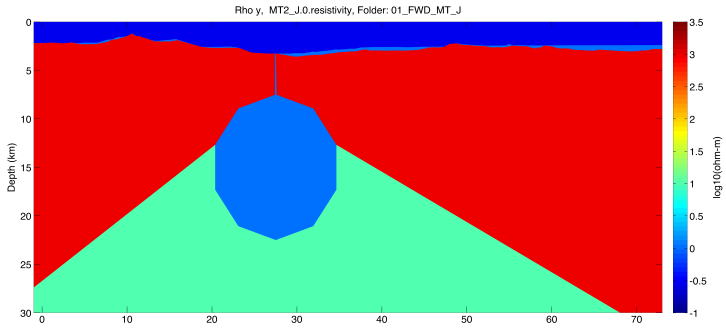

(a) Start model for large scale MT and CSEM forward modelling.

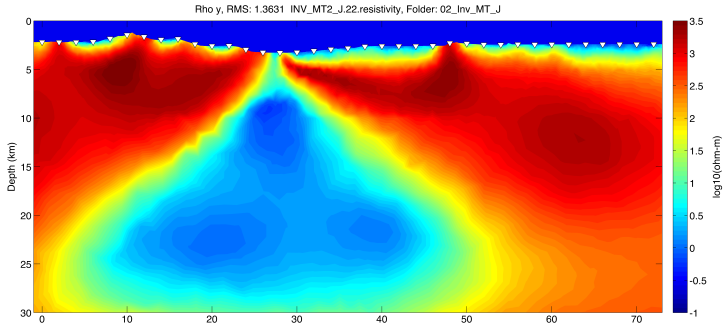

(b) Large scale MT inversion resistivity model. Misfit of 1.3631 after 22 iterations.

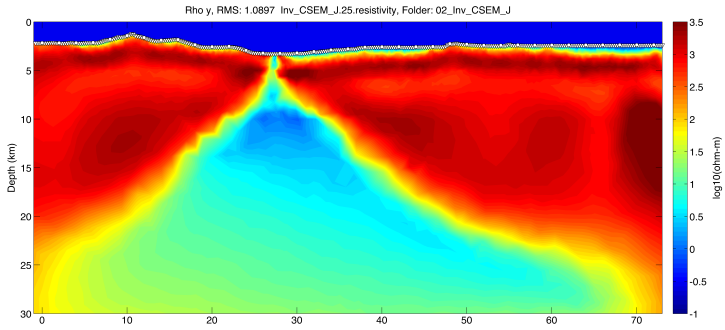

(c) Large scale CSEM inversion resistivity model. Misfit of 1.0897 after 25 iterations.

Figure 4.3: Large scale resistivity model and inversion. Red colours are resistive, blue are more conductive.

4.3 Imaging of SMS deposits

From **Fig. 4.4**, the background model and the start model for SMS deposits are shown, whilst in **Fig. 4.5** the blue curve represents the background model without any SMS deposits, while the red dashed curve are from the model with conductive SMS targets, both for receiver position 70 km for 0.5 Hz. On the right side of the magnitude plot (top), there are no conductive anomalies which lead to both curves being smooth and reading the same values. The phase curve (bottom) shows the same trend for the right side. On the left side, however, considering the magnitude plot, there are two distinctive spikes in the red dashed data at 55 km and 59 km. There is also possible to see small separations of the two curves where the red dashed curve loses magnitude compared to the blue curve at 58 km, 62 km, and 66 km. The same separation of the curves is easier spotted in the phase shift plot for the same positions, where the red dashed curve loose phase velocity compared to the background model, indicating more attenuation.

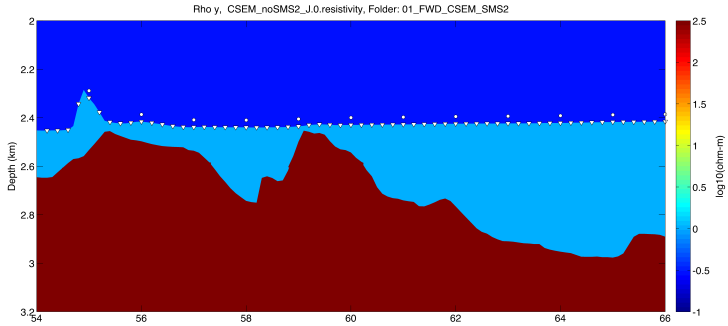

(a) Start model for background model without SMS deposits.

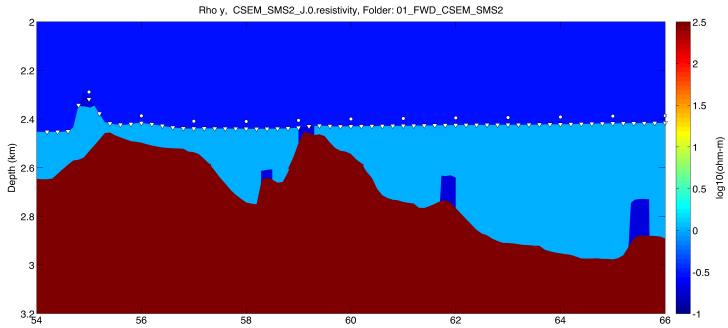

(b) Start model for large SMS deposits.

Figure 4.4: Magnitude plot (top) and phase shift (bottom) data from CSEM modelling. Red curve represents data from model with SMS mounds, blue curve represents background model without SMS.

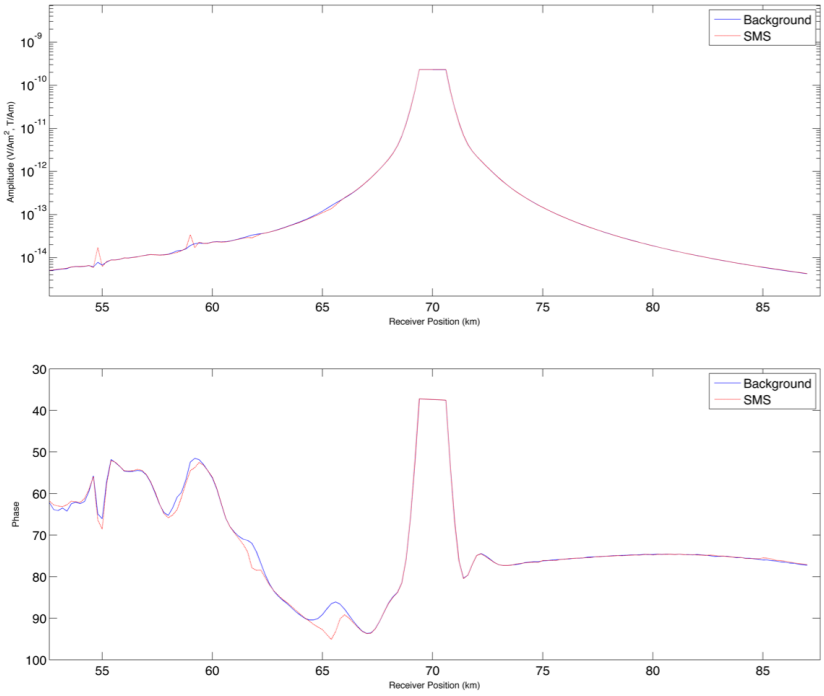

Figure 4.5: Magnitude plot (top) and phase shift (bottom) data from CSEM modelling. Red curve represents data from model with SMS mounds, blue curve represents background model without SMS.

To clarify the geometry of the SMS deposits in **Fig. 4.7a** and in **Fig. 4.8a**, which look like pillars, **Fig. 4.6** shows how the SMS mounds look like on an equal axis. This is the SMS deposit furthest to the right and this is the largest one from **Fig. 4.7a**.

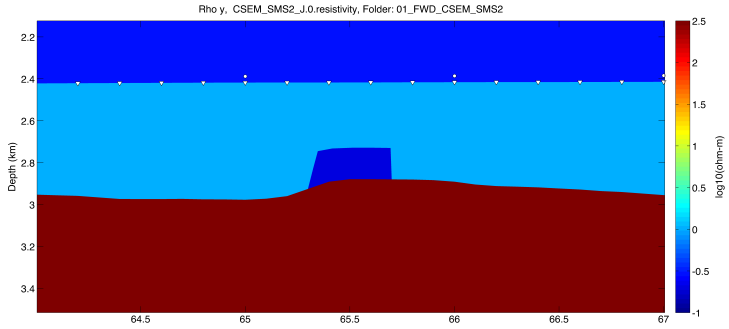

Figure 4.6: Geometry of SMS mounds on equal axis.

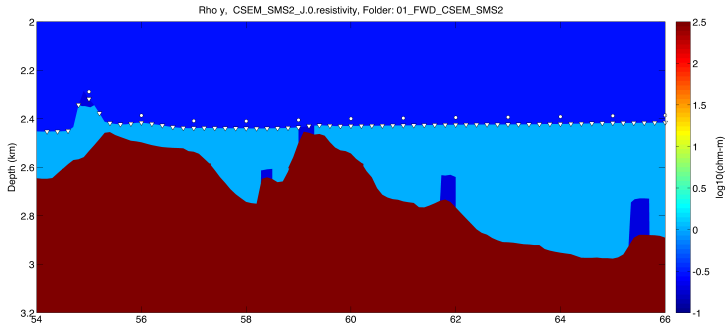

(a) Start model of large SMS deposits.

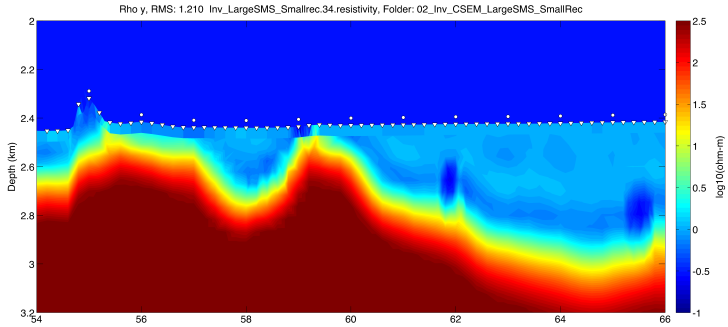

(b) Inverted resistivity model for large SMS deposits. Misfit of 1.210 after 34 iteration.

Figure 4.7: Large SMS depoits inverted (b) from model (a).

4.3.1 Impact of Size of SMS deposits on the Imagability

In the model of **Fig. 4.7a**, the SMS deposits are made deliberately large, reaching from 55 m to almost 200 m in height and from 200 m to 400 m in length. This was to ensure that it was possible to get the wanted response from the CSEM inversion. Two of the targets are on the seafloor whilst three are buried under sediments. For the modelling and inversion, 33 receivers were used between 40 km and 72 km resulting in a receiver spacing of 1 km. Seven frequencies, 0.5 Hz, 1.0 Hz, 2.0 Hz, 4.0 Hz, 8.0 Hz, 16.0 Hz and 32.0 Hz, was used to obtain the resistivity distribution in **Fig. 4.7b**. The total misfit ended at 1.210 after 34 iterations.

For the model used in **Fig. 4.8**, the SMS deposits were made smaller, from 35 m in height and 65 m in length to 100 m in height and 200 m in length. This was to see how small the deposits can be in order to successfully give a conductive anomaly on the inverted data. The same receiver spacing and frequency content were used as for the larger SMS deposits to make them more comparable. After 12 iterations the inversion model converged towards a misfit of 1.364.

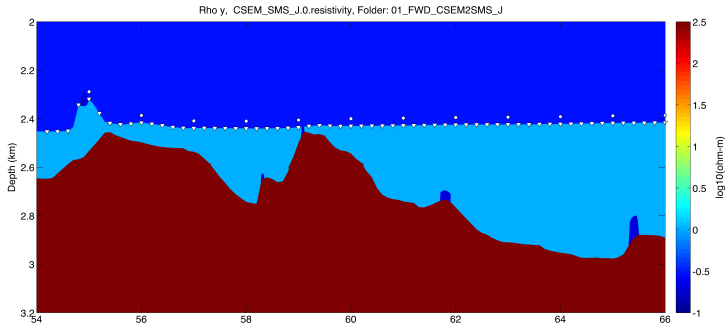

(a) Start model for small SMS deposits.

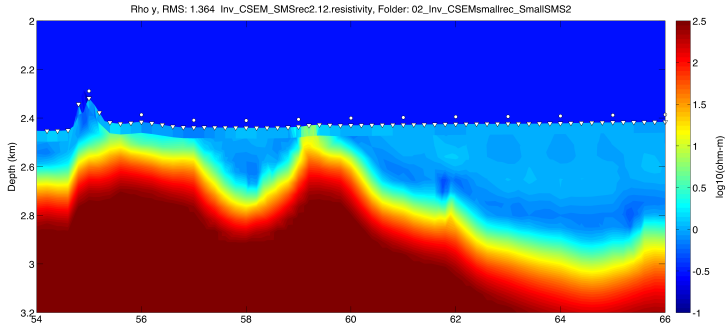

(b) Inverted resistivity model for small SMS. Misfit of 1.364 after 12 iterations.

Figure 4.8: Small SMS deposits inverted (b) from model (a).

Fig. 4.9 is the comparison of the inversion results between large SMS deposits, **Fig. 4.9a**, and small SMS deposits, **Fig. 4.9b**. It is easily spotted a difference in the intensity of the conductive anomalies in the two plots.

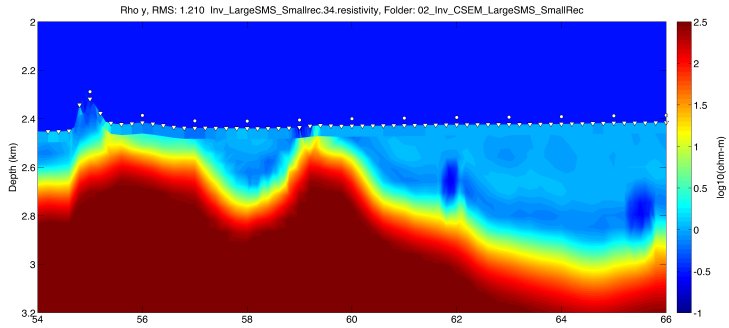

(a)

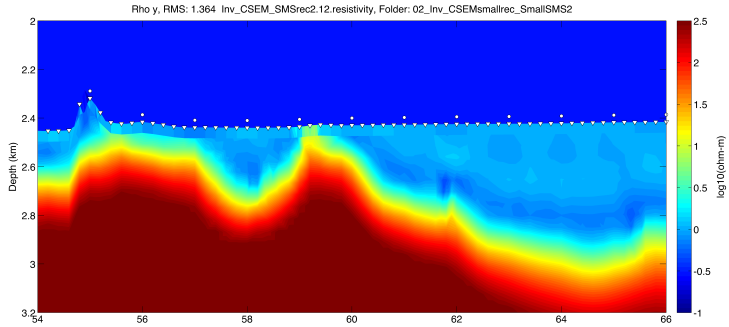

(b)

Figure 4.9: Comparison of inverted resistivity models for large SMS deposits (a) and small SMS deposits (b).

4.3.2 Impact of Frequency content of the CSEM Signal on Imaging Sensitivity

In **Fig. 4.10** a comparison between the large SMS case, **Fig. 4.10a**, a low frequency only case, **Fig. 4.10b**, and a high frequency only case, **Fig. 4.10c**, has been made. All the inversion models have the same receiver spacing, 1 km, but they have different frequency content. For the large SMS case, still all seven frequencies were used, but for the low frequency case, only four frequencies, 0.25 Hz, 0.5 Hz, 1.0 Hz and 2.0 Hz was used. This resulted in 25 iterations where the model converged towards 1.152 in misfit. For the high frequency case, four high frequencies were used, 4.0 Hz, 8.0 Hz, 16.0 Hz and 32.0 Hz, and the model converged at 1.145 after 30 iterations. There is a distinct difference in the low frequency plot and high frequency plot as the colours in the low frequency plot are much more smeared out than for the two other cases.

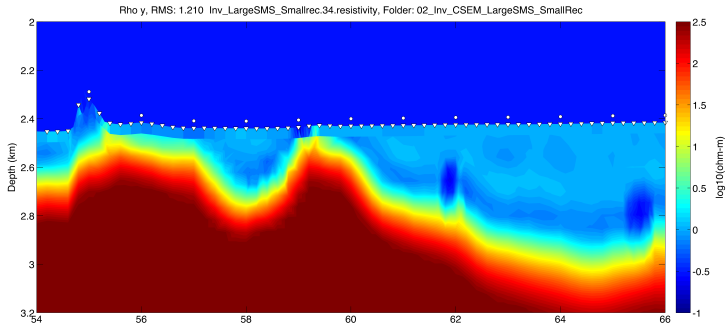

(a) Inverted resistivity model for large SMS as reference.

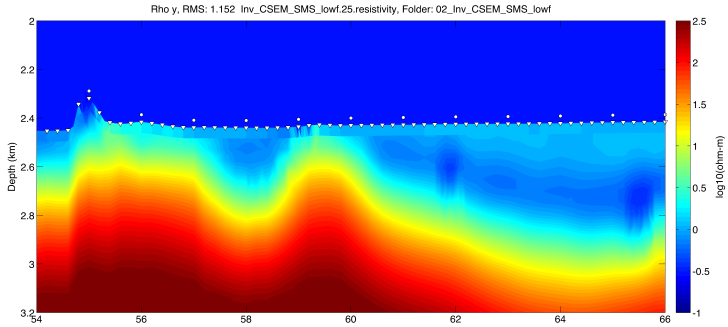

(b) Low frequency inverted resistivity model.

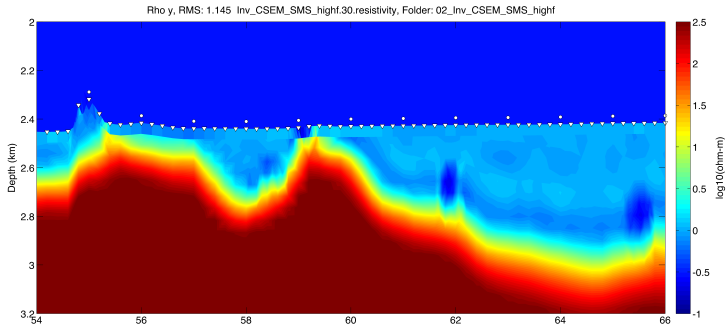

(c) High frequency inverted resistivity model.

Figure 4.10: Frequency dependent inversion results.

4.3.3 Impact of Survey Geometry on Imaging Sensitivity

It is also reasonable to look at the survey geometry. Since closer receiver spacing usually would lead to better data, but there is a trade-off between how good your data need to be compared to the cost of the survey. The more receivers one need, the more it will cost to do the survey. In **Fig. 4.11**, a comparison of the large SMS case with 1 km receiver spacing, **Fig. 4.11a**, 2 km receiver spacing, **Fig. 4.11b**, and 750 m receiver spacing **Fig. 4.11c** is done. In this test, only the receiver spacing parameter is changed, all others are the same. Same size of SMS targets and the same frequencies are used. In the 2 km spacing case, the conductive anomalies are not that much different from the 1 km spacing case, but a small difference in the 59 km seafloor anomaly. The 2 km inversion model converged after 18 iterations towards 1.236 in misfit. In the 750 m receiver spacing test one can almost spot a fifth anomaly around 58 km. This test converged at a misfit of 1.1643 after 20 iterations.

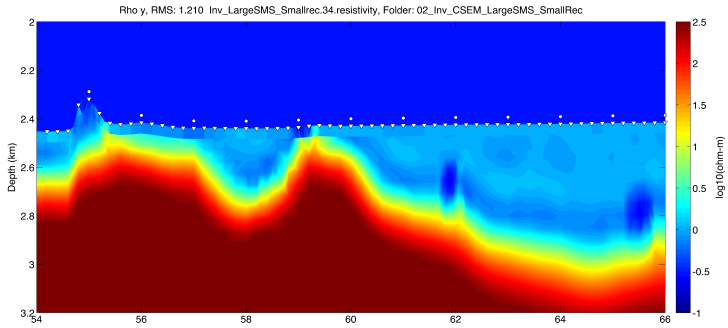

(a) Inverted resistivity model for large SMS as reference.

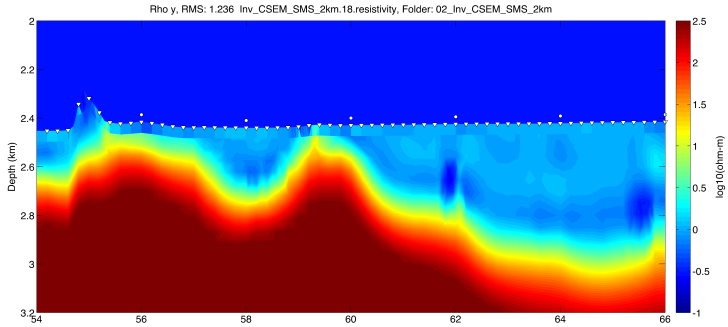

(b) Inverted resistivity model for 2 km receiver spacing.

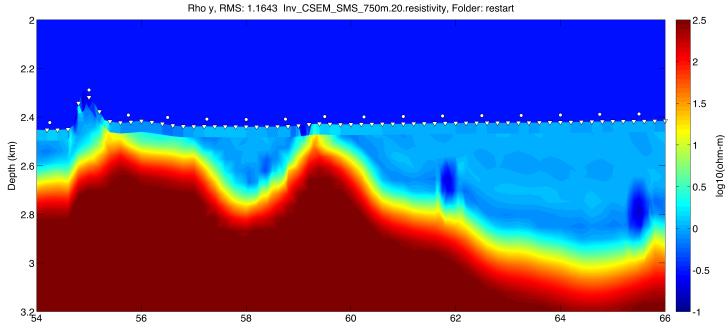

(c) Inverted resistivity model for 750 m receiver spacing.

Figure 4.11: Receiver spacing dependent inversion results.

Chapter 5

Discussion

In this chapter, the results of the synthetic forward modelling and inversion study will be discussed, but also what is done before of similar research with similar methods. The ability of marine CSEM and MT to reconstruct the subsurface resistivity structure of a mid-ocean ridge will be discussed. Further, the ability of CSEM to image and detect SMS deposits of different size and at different depths will be discussed, and the EM methods used are set in context with other geophysical methods. A part with suggestions for further work will also be presented.

5.1 Discussion of results

5.1.1 Ability of MT to Resolve a Deep Magma Chamber

Fig. 4.2 of the different MT modes showed a separation in the apparent resistivity for both modes at around $10^2 s$. For a resistive background, like the blue curve, it will increase towards $10^3 \Omega m$ which is the dominating subsurface resistivity of the model. An influence of a more conductive body in the subsurface, **Fig. 4.1b**, will decrease the apparent resistivity value, since it is an average of the subsurface resistivity, and a separation between the red and blue curve is spotted:

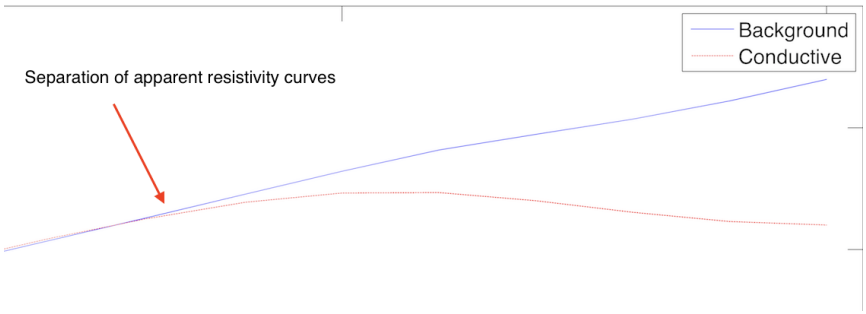

Figure 5.1: Illustration of separation in the apparent resistivity curve for large scale MT modelling. Conductive model represented by red curve and resistive background model respresented by blue curve.

For the impedance phase, which is an indication of phase velocity, low phase angles indicate high resistivity and large phase velocities. This would be the case for the resistive background model represented by the blue curve. The red curve, however, shows larger phase angles, which indicates more attenuation and lower phase velocities, **Fig. 5.2**. This is a typical case for a more conductive subsurface, as higher conductivity leads to larger attenuation of the signal. Both separation of the apparent resistivity and the impedance phase are spotted on the TM and TE modes.

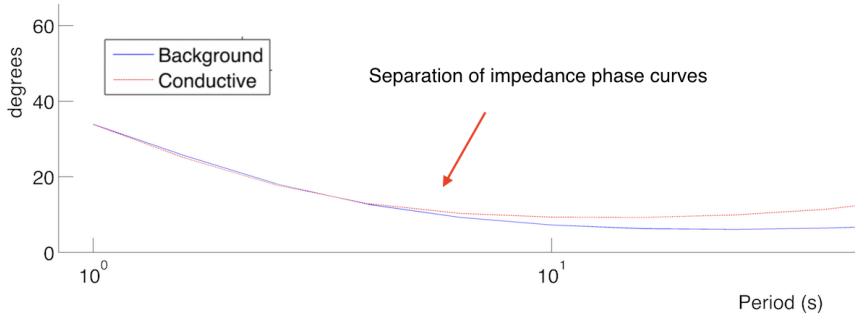

Figure 5.2: Illustration of separation in the impedance phase curve for large scale MT modelling. Conductive model represented by red curve and resistive background model respresented by blue curve.

In **Fig. 4.3** the goal was to image the model of a magma chamber with a partial melt below from MT and CSEM forward modelling and inversion. MT with its low frequencies and long skin depth have the ability to image structures at large depths better than CSEM. The conductive zones on the MT inversion model are well imaged in the deep, especially around 10-20 km depths, but below the magma chamber, it struggles to resolve where the magma chamber stops and becomes a less conductive partial melt. This could be due to large attenuation in the very conductive magma chamber. Also, for shallower depths, it struggles to give good enough resolution. The magma feeder that goes from the chamber towards the seafloor is imaged to large, and the boundary between sediments and base-

ment don't have a well-defined transition. A lack of higher frequencies gives only large wavelengths and poor resolution. In the CSEM case, the almost opposite effect can be seen. CSEM with its higher frequency content can resolve the feeder and the transition between sediments and basement much better than MT, but it has a shorter skin depth and it struggles to even detect the full conductivity anomaly of the magma chamber. For this test, small enough frequencies were used to image some of the deeper parts, and the partial melt part is actually quite decent imaged, even if it isn't able to separate the magma chamber and the partial melt from each other.

5.1.2 Imaging and Data Sensitivity for SMS deposits

From the CSEM modelling of the SMS deposits between 54 km and 66 km, it is possible to generate the same comparison as for the MT case with and without conductive bodies. Five SMS mounds were inserted into the model, where two were on the seafloor, whilst three were buried beneath sediments. From the magnitude plot in **Fig. 4.5** it is possible to see two spikes in the red data curve at 55 km and 59 km, which is where the two SMS mounds that are located on the seafloor are found in the model. The three buried SMS mounds can be seen as a small separation in the blue background curve and the red SMS modelled data curve, **Fig. 5.3**. The separation is due to a reduction in magnitude from attenuation in the conductive bodies compared to the less conductive surroundings. Notice that on the right side of the curve, the curve is smooth and no separation can be seen as there is no difference in resistivity values for the two cases.

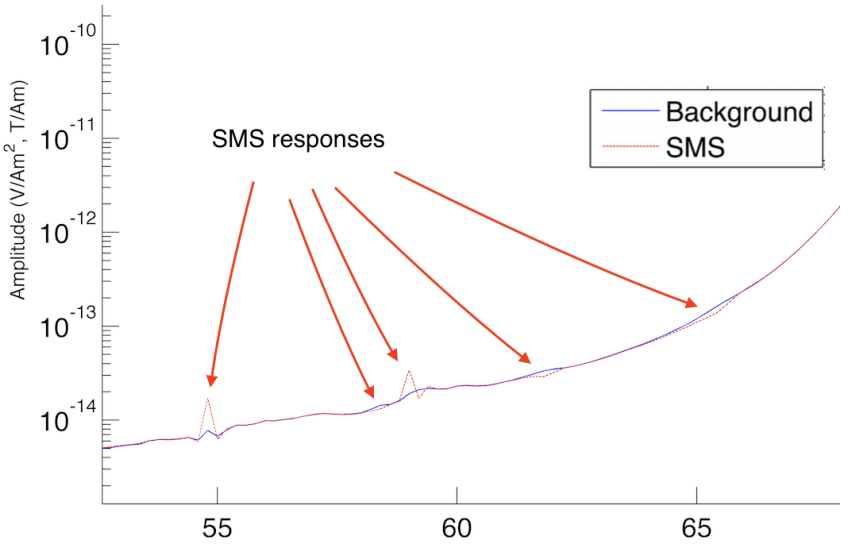

Figure 5.3: Magnitude plot where spikes and separations between the two models represent SMS mounds.

Attenuation due to conductive bodies is also reflected in the phase shift curve, and

in this case, it is easier spotted from the phase curve than the magnitude curve. More attenuation due to conductive bodies leads to higher phase angles and a reduction in the phase velocity. This can be seen in the separations marked with red arrows in **Fig. 5.4** where the model with SMS targets have a lower phase velocity than the background model.

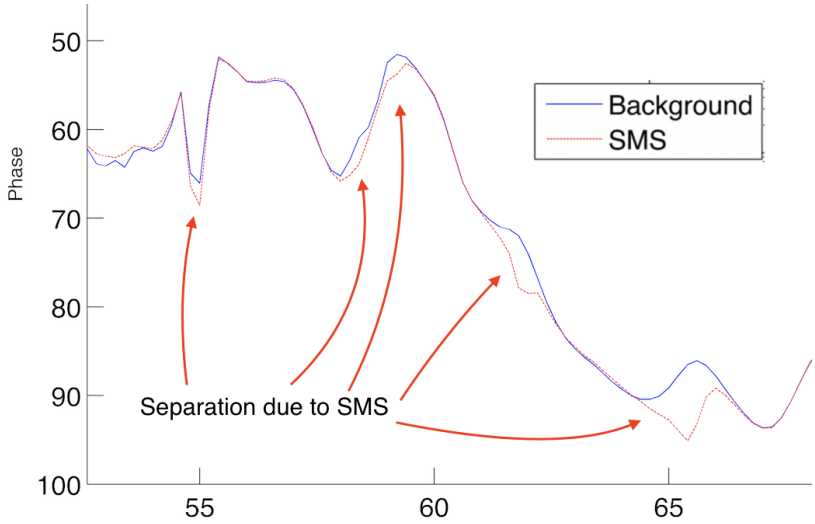

Figure 5.4: Phase shift plot where the separation indicates conductive SMS targets.

One of the main goals of the thesis is to investigate how well inversion of CSEM data can reconstruct SMS deposits in the subsurface. For the first case involving SMS, **Fig. 4.7**, four conductive anomalies are clearly visible. The two on the seafloor and the two largest SMS mounds to the right were successfully imaged from the inversion, but the smaller mound at 58 km is not visible. A combination of the size of the mound and that it is buried beneath sediments is most likely an explanation. What else that may be noticed is that the transition between sediments and basement are well imaged in this case (all frequencies), but also here it fails to image the small ”bump” of the basement that the un-imageable SMS mound is located. This could be due to resolution issues.

5.1.3 Impact of size of SMS on Imaging Quality

For the next test, all the parameters were the same, except the size of the SMS mounds, which were smaller. **Fig. 4.8** shows the resistivity distribution after modelling and inversion of the small SMS deposits. Like for one of the smaller SMS mounds in **Fig. 4.7**, they are hard to image. The only mound that is somehow decent imaged is the SMS at 55 km which is on the seafloor. The rest of the conductive anomalies are really poorly imaged, and it is only the SMS at 62 km of the buried ones that has given some anomaly that could be of interest. This test confirms more or less the doubt from the previous test when it comes to the size of the deposits. It seems that the mounds need to be of a certain size in order to be properly imaged by CSEM, at least if they are buried beneath sediments. This

is easily seen from **Fig. 4.9**, where there are four clear anomalies for the large SMS case and only one obvious and one tiny anomaly buried by sediments.

5.1.4 Impact of CSEM frequencies on resolution

In the frequency dependent test, the size of the mounds was held constant, as well as the receiver spacing. Three test are compared, one with all seven frequencies [0.5 Hz, 1.0 Hz, 2.0 Hz, 4.0 Hz, 8.0 Hz, 16.0 Hz and 32.0 Hz], one with four low frequencies [0.25 Hz, 0.5 Hz, 1.0 Hz, 2.0 Hz] and one with four high frequencies [4.0 Hz, 8.0 Hz, 16.0 Hz, 32.0 Hz]. At first glance, **Fig. 4.10a** and **Fig. 4.10c** looks very similar. They have both two conductive anomalies for the seafloor bound mounds and two conductive anomalies for the buried mounds, and both figures show a good and clear interface between sediments and the basement. The only part that separates the two inversion results is that for the high frequency case, the SMS mound at 58 km which is not imaged for all frequencies, gives a small anomaly for high frequencies only. Looking at the difference in misfit of the two, the high frequency only case has a lower misfit and is, therefore, closer to the actual model than the all frequency case, **Fig. 5.5**.

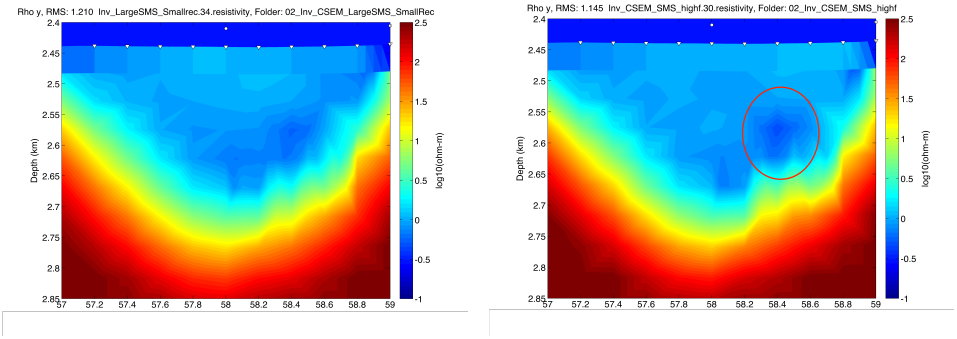

(a) All frequencies.

(b) High frequencies only.

Figure 5.5: Small anomaly for the high frequency case (b) compared to all frequency case (a). Red circle indicates where there is a small change in conductive anomaly for SMS mound at 58 km.

On the low frequency case, **Fig. 4.10b**, the first one notice is how poor the transition between sediments and basement are imaged. The low frequencies don't have the resolution to sharply map the transition due to long wavelengths and a diffuse transition can be seen:

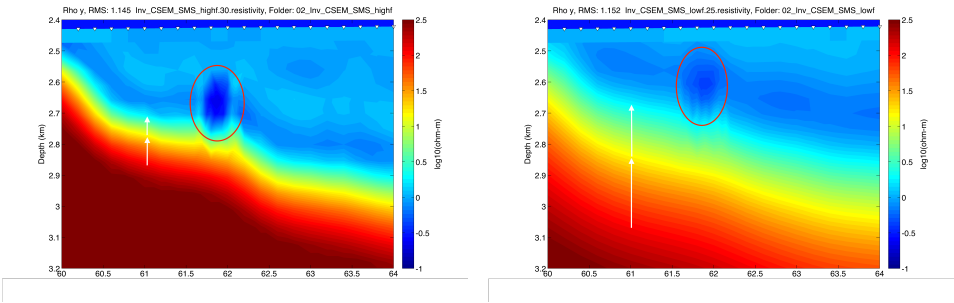

(a) High frequencies.

(b) Low frequencies.

Figure 5.6: A sharp contrast between the sediments and basement for the high frequency case (a), but the transition is poorly mapped from the low frequency case (b). White arrows show the thickness of the transition of the sediment-basement interface, placed right above the 61 km mark. The red circle indicates the different position of the SMS anomaly and also how much less dense the anomaly is for low frequencies only compared to high frequencies. Horizontal scale in km away from the start of the line.

Another feature to take a look at is how much denser the high frequency anomaly for the buried mounds are compared to the low frequency anomalies. They display the same effect as for the transition of the interface, a diffuse conductive anomaly. which also can be seen in **Fig. 5.6**. Not only to mention that for low frequencies, it also struggles to image the depth of where the anomaly lies. For all frequencies and high frequencies only the anomaly at 62 km lies right below 2.6 km in depth, which is where it lies from the forward model, but for low frequencies, it is imaged directly at 2.6 km depth. Correct depth placement and volume estimates are a major concern for mining after these types of deposits.

5.1.5 Impact of Receiver Separation on Imagibility

The last test that was performed was different receiver spacing when SMS mound size and frequency content was held constant. In the reference case, **Fig. 4.11a**, 1 km receiver spacing is used and is compared to **Fig. 4.11b** where 2 km receiver spacing is used. Only minor changes in the resistivity distribution can be spotted. The sediment-basement interface is a bit more diffuse for the 2 km spacing case, but not in the same way as for low frequencies, which showed a remarkable difference. The 2 km spacing test struggles to image one of the SMS mounds at the seafloor at 59 km compared to the 1 km spacing test. A closer look at the receivers shows that for 1 km spacing, the mound has a receiver almost right above it, but that the mound falls in between two receivers for the larger spacing test. The signal that reaches the SMS mound is, therefore, more attenuated when the distance to the receiver is longer, and will, therefore, be more difficult to retrieve the right conductive anomaly.

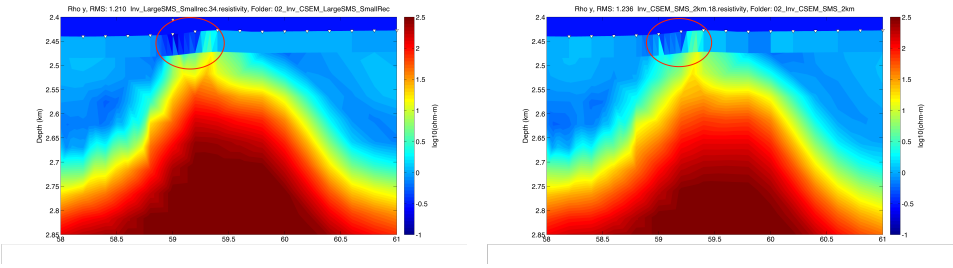

(a) 1 km receiver spacing. **(b)** 2 km receiver spacing.

Figure 5.7: Difference in conductive anomaly for the SMS mound at the seafloor at 59 km. For 1 km case (a), the mound has a receiver right above it (receiver each km), but in the 2 km test (b) the mound falls in between two receivers (only each 2 km, at 58 km, 60 km etc.).

The final comparison was with a receiver spacing of only 750 m, **Fig. 4.11c**. Compared to the 2 km spacing test, 750 m receiver spacing resolves the interface between sediments and basement to a sharper transition. It also enhances the imaging of the SMS mound at 59 km better. Compared to the 1 km test, there are minor differences. Small differences in the transition at the interface, but more interesting there are some changes in both the SMS mound at 59 km, but also for the one at 58 km. As **Fig. 5.8** shows, the 750 m spacing concentrates the SMS mound anomaly at 59 km to a smaller area and narrows down the possible location of the mound. It does also produce a slightly more conductive anomaly for the buried mound at 58 km compared to the 1 km case and makes it more comparable with the inversion result for high frequencies, **Fig. 5.5**, for this particular mound.

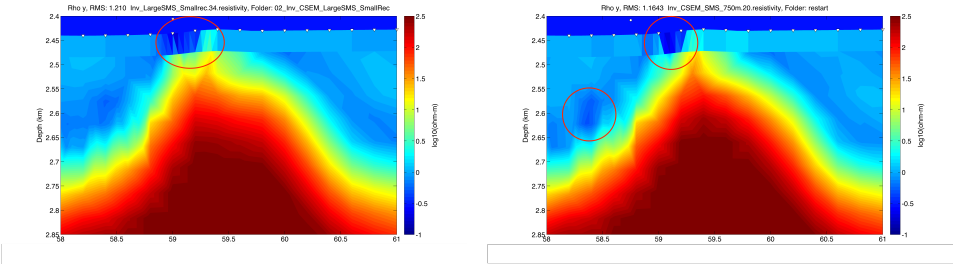

(a) 1 km receiver spacing. **(b)** 750 m receiver spacing.

Figure 5.8: Red circles indicates differences in conductive anomalies for the SMS mounds at 58 km and 59 km for 1 km spacing (a) and 750 m spacing of receiver (b).

To summarise the EM imaging results, MT works well for imaging of deep and large structures but struggles with resolution in the shallower parts of the model. CSEM don't have the penetration depth as MT but resolves the shallower subsurface much better than MT. From MT data analysis it was possible to see that conductive subsurface features would provide sufficient changes in resistivity to influence the apparent resistivity and the impedance phase for the subsurface model.

For the tests done with SMS mounds, it was shown that the SMS deposits need to be of a certain size to be imaged. The small ones were hard to image, and only the ones at the seafloor gave any conductive anomalies. From CSEM data analysis it was obvious that the spikes in the magnitude plot were related to the SMS mounds found on the seabed. The same spikes are found when towing CSEM above pipelines on the seabed. The separation of the magnitude curves is due to an attenuation effect given by the conductive targets.

For the frequency comparison, larger frequencies replicate the true model more accurately than low frequencies. It has smaller wavelengths and is able to resolve smaller targets better than large wavelengths and low frequencies.

Survey planning is an important part of the feasibility study and with that the receiver spacing geometry. This is a trade-off between how good the subsurface resistivities can be reconstructed, and how much money that can be used on the survey. The results are not that much different, but small receiver spacing means more data that describes the subsurface and therefore gives a better reconstruction of the resistivity model.

5.2 Earlier work and method

For the large scale magma chamber modelling and inversion, there are several papers on the subject, and Key et al. (2013) was a heavy influence for the test of MT modelling and inversion. When it comes to CSEM modelling and inversion of the SMS mounds, some simplified modelling has been done earlier with more focus on the used method rather than for an exploration purpose, (Kowalczyk et al., 2015; Imamura et al., 2011, 2012). For this thesis, it has been done a large scale modelling and inversion after SMS deposits for mineral exploration purposes, with geology from an expected SMS environment together with real case acquisition parameters. This separates the thesis and results from most of the other papers that have been written on the subject. The results are therefore interesting and also important pre-survey work in order to know which parameters that is most suitable in a real case scenario.

The whole project and test are done through 2D modelling and inversion, and not 3D. Geology is as everyone knows in 3D and will be a lot more complicated when taking all survey parameters into account with receiver grid and towlines, but also that there are even more directions in the subsurface to record data from. In a 2D case, it is assumed that the model that is created works infinite inward, which is not the case. 3D modelling and inversion can limit the inward contribution of e.g. the SMS mounds. Also, the tests are done based on isotropic conditions, which is not likely to be a real life scenario at the Atlantic Mid-Ocean Ridge, but it is a sufficient assumption for studying imageability and sensitivity. The model is also very simplified with only one resistivity value for all the sediments that lies above the basement, and there is not taken into account for the different facies inside the basement, i.e. dykes and pillow lavas and any other geological features before the magma chamber and the partial melt below. For the SMS mounds, a single resistivity value was chosen as well, and the model only included the mounds itself, and not chimneys, stockwork zones or zonation of the different minerals within the mound. The transmitters are also the same height above the seafloor everywhere in the model, but due to the complex geology at the mid-ocean ridge, which is used in the model, and length of the transmitter, a more smooth towpath above the largest geological features on the

seafloor needs to be taken.

Still, the results of the test are valid and give a lot of insight. Compared to seismic, CSEM has lower resolution and will retrieve an average signal from a larger area than e.g. seismic, which means that it is the ”bigger picture” that is looked for. A simplification of the SMS mounds is therefore not the biggest issue with the method. A concern for a real case scenario will anyways be the resolution of CSEM. CSEM normally uses much lower frequencies than seismic. For this project, frequencies up to 32 Hz is used, but that is still only half of what is normal for seismic, and 32 Hz in CSEM is a pretty high frequent CSEM survey. Hence, seismic has the resolution to detect smaller SMS deposits due to shorter wavelengths. Another dilemma with imaging using EM methods is that an image of the subsurface is retrieved through inversion. And as stated in the theory chapter, it is an ill-posed problem, which means it is not unique. There are several solutions, or models, that fits the data. This may, of course, be dealt with through regularisation and roughness penalties added to the inversion criteria, which will push the inversion model into the right direction, but still, non-uniqueness still exists.

Advantages of the method are that CSEM is sensitive to changes in resistivity, and not impedance contrasts like seismic. That is advantageous taking into account that SMS deposits are build up by conductive minerals that are found in volcanic environments, which are very resistive. The high contrasts in impedance between sediments or seawater and the volcanic basement are often so large that the seismic signal is scattered, and not able to see into or below the volcanic rocks, see **Fig. 5.9**. EM methods don’t have that issue, as resistive formations reduce the attenuation and enhance the penetration depth of the signal. In very complex geological areas it is also possible to take CSEM measurements by using two autonomous underwater vehicles (AUV), one as a source and one as a receiver, to avoid cable tangling (Imamura et al., 2011).

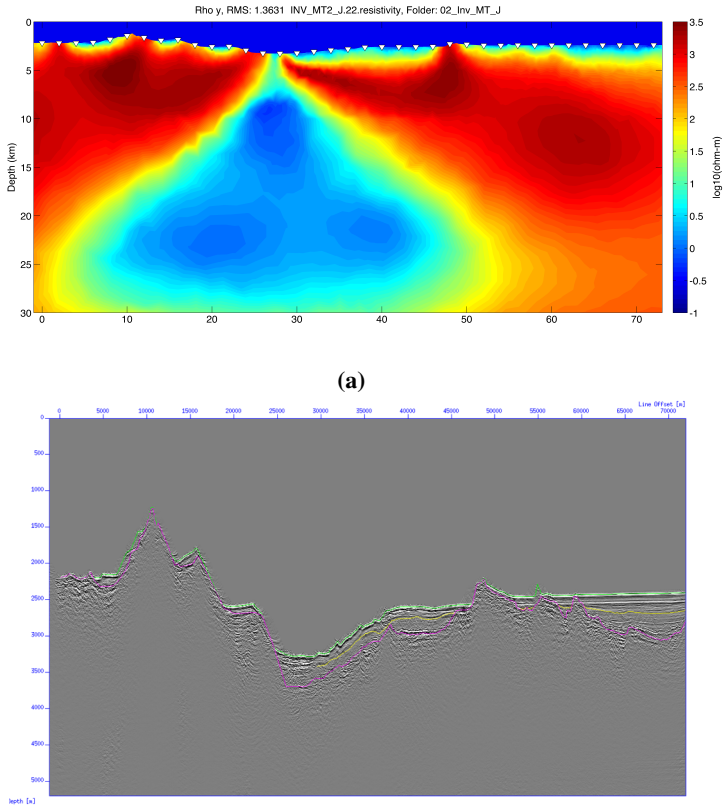

(a)

(b)

Figure 5.9: Comparison of inverted resistivity models for MT (a) and seismic section (b) of the same area. Seismic signal scattered right below the basement, whilst MT can image deep beneath the top basement. Also showing seismic horizons that were used to create the forward start model. Top basement in purple, a sediment layer in yellow and seafloor in green.

5.3 Further work

There are a lot of opportunities when it comes to marine mineral exploration after SMS, and still a lot of unanswered questions. One that is recommended for modelling and inversion is to take into account the circulating seawater that creates these deposits. Seawater is in itself conductive, and whilst containing metal minerals that are leached from the surrounding rocks it should be even more conductive. How will the circulating seawater change the inversion model? Will it make such a contribution to conductive anomalies that it will mask the SMS deposits, or maybe it will give a clue of where to locate the deposits? Maybe it will be an important part of the exploration strategy in the future, or maybe the contribution on changes in resistivity is of a scale that is negligible.

3D forward modelling and inversion would also be interesting to look at. The geology at the mid-ocean ridge is complex and a 3D response of the mounds will be limited in all directions, R(x,y,z), instead of only the observation plane and in depth, R(x,z), like in this study. Perhaps even larger SMS mounds are necessary in order to detect them with CSEM.

It would also be interesting to look at the induced polarization (IP) effect on the SMS deposits. Either by including the IP effect when modelling and inverting EM data, or just by itself. Maybe there are other methods that work a lot better to explore after SMS deposits than CSEM.

Chapter 6

Conclusion

This project has shown that:

- MMT is a good tool to image deep mantle structures.
- Spikes on a magnitude plot means SMS deposits on the seabed, and separation means they are buried beneath sediments.
- The buried SMS mounds needs to be of a significant size in order to be able to image. Preferably larger than 60 m in height and 200 m in length. At the seabed, smaller deposits can be detected.
- Low frequencies struggle to define the interface between sediments and basement and misplace the mineral mounds.
- High frequencies are preferable as it enhances the resolution and detection of mineral mounds.
- Receiver spacing is not essential to alter the outcome of inversion, but shorter receiver spacing adds accuracy to the inverted resistivity model.

The tests have shown that CSEM is a valuable tool when it comes to a large scale exploration after seafloor massive sulphide deposits in deep sea environment.

There were issues with imaging of ”smaller” buried mounds, which were hard to spot from the inverted resistivity model. Also, anisotropic conditions, a more detailed resistivity model, and 3D modelling and inversion may alter the results of these tests.

For future work, a model with seawater circulation pattern should be taken into consideration. A 3D forward modelling and inversion study should also be considered for further work as it would give a more realistic representation of the geology and the geophysical response of the targets.

These results can work as a part of a feasibility to a real case CSEM survey and may provide valuable information before choosing survey parameters.

References

Bhuiyan, A. H., Wicklund, T. A., Johansen, S. E., 2006. High-resistivity anomalies at modgunn arch in the norwegian sea. First Break 24 (1), 39–44.

Bhuyian, A. H., Thrane, B. P., Landrø, M., Johansen, S. E., 2010. Controlled source electromagnetic threedimensional gridmodelling based on a complex resistivity structure of the seafloor: effects of acquisition parameters and geometry of multilayered resistors. Geophysical Prospecting 58 (3), 505–533.

Boschen, R. E., Rowden, A. A., Clark, M. R., Gardner, J. P. A., 2013. Mining of deep-sea seafloor massive sulfides: A review of the deposits, their benthic communities, impacts from mining, regulatory frameworks and management strategies. Ocean and Coastal Management 84, 54–67.

Chave, A. D., Constable, S. C., Edwards, R. N., 1991. Electrical exploration methods for the seafloor. Electromagnetic methods in applied geophysics 2, 931–966.

Conley, M. M., Dunn, R. A., 2011. Seismic shear wave structure of the uppermost mantle beneath the mohns ridge. Geochemistry, Geophysics, Geosystems 12 (10).

Constable, S., Srnka, L. J., 2007. An introduction to marine controlled-source electromagnetic methods for hydrocarbon exploration. Geophysics 72 (2), WA3–WA12.

Eidesmo, T., Ellingsrud, S., Farestveit, A., Johansen, S. E., Pedersen, H., Eidesmo, T., 2009. Method and apparatus for determining the nature of submarine reservoirs. US Patent 7 (567), 084.

Eidesmo, T., Ellingsrud, S., MacGregor, L. M., Constable, S., Sinha, M. C., Johansen, S. E., Kong, F. N., Westerdahl, H., 2002. Sea bed logging (sbl), a new method for remote and direct identification of hydrocarbon filled layers in deepwater areas. First break 20 (3).

EM-GeoSci, 05.06.17. `http://em.geosci.xyz/content/geophysical_surveys/mt/index.html`. GeoSci Developers.

Glasby, G., 2002. Deep seabed mining: Past failures and future prospects. Marine Georesources & Geotechnology 20 (2), 161–176.

Hannington, M. D., 2014. Volcanogenic massive sulfide deposits. Treatise on Geochemistry 2nd Edition. Edited by HD Holland, and Turekian, KK Elsevier Ltd, 319–350.

Hekinian, R., 2014. Sea floor exploration : Scientific adventures diving into the abyss. Springer Oceanography, 152.

Hoagland, P., Beaulieu, S., Tivey, M., Eggert, R., German, C., Glowka, L., Lin, J., 2010. Deep-sea mining of seafloor massive sulfides. Marine Policy 34 (3), 728–732.

Imamura, N., Goto, T., Takekawa, J., Mikada, H., 2011. Application of marine controlled-source electromagnetic sounding to submarine massive sulphides explorations. SEG Technical Program Expanded Abstracts 30 (1), 730–734.

Imamura, N., Goto, T., Takekawa, J., Mikada, H., 2012. Full time-domain waveform inversion of controlled-source electromagnetic exploration of submarine massive sulphides. SEG Technical Program Expanded Abstracts 2012, 1–6.

Johansen, S. E., Amundsen, H. E. F., Rsten, T., Ellingsrud, S., Eidesmo, T., Bhuiyan, A. H., 2005. Subsurface hydrocarbons detected by electromagnetic sounding. First Break 23 (3), 31–36.

Johansen, S. E., Gabrielsen, P. T., 2015. Interpretation of marine csem and marine mt data for hydrocarbon prospecting. Petroleum Geoscience: From Sedimentary Environments to Rock Physics, 515–544.

Johansen, S. E., Wicklund, T. A., Amundsen, H. E. F., 2007. Interpretation example of marine csem data. The Leading Edge 26 (3), 348–354.

Key, K., 2012a. Marine electromagnetic studies of seafloor resources and tectonics. An International Review Journal Covering the Entire Field of Geosciences and Related Areas 33 (1), 135–167.

Key, K., 2012b. Marine em inversion using unstructured grids: a 2d parallel adaptive finite element algorithm. SEG Technical Program Expanded Abstracts 2012, 1–5.

Key, K., Constable, S., Liu, L., Pommier, A., 2013. Electrical image of passive mantle upwelling beneath the northern east pacific rise. Nature 495 (7442), 499–502.

Kowalczyk, P., Bloomer, S., Kowalczyk, M., 2015. Geophysical methods for the mapping of submarine massive sulphide deposits. Offshore Technology Conference held in Houston, Texas, USA, 47 May 2015.

MARE2DEM, 06.06.17. http://mare2dem.ucsd.edu. University of California San Diego.

Myer, D., Constable, S., Key, K., 2013. Magnetotelluric evidence for layered mafic intrusions beneath the vring and exmouth rifted margins. Physics of the Earth and Planetary Interiors 220, 1–10.

Naidu, G. D., 2012. Magnetotellurics: Basic theoretical concepts. Deep Crustal Structure of the Son-Narmada-Tapti Lineament, Central India Springer, 13–35.

NOAA, 05.06.17. http://oceanexplorer.noaa.gov/explorations/02fire/background/hirez/chemistry-hires.jpg. U.S. Department of Commerce - Office of Ocean Exploration and Research.

Petersen, S., Herzig, P. M., Hannington, M. D., 2000. Third dimension of a presently forming vms deposit: Tag hydrothermal mound, mid-atlantic ridge, 26n. nternational Journal of Geology, Mineralogy and Geochemistry of Mineral Deposits 35 (2), 233–259.

Petersen, S., Krtschell, A., Augustin, N., Jamieson, J., Hein, J. R., Hannington, M. D., 2016. News from the seabed geological characteristics and resource potential of deep-sea mineral resources. Marine Policy 70, 175–187.

Røsten, T., Johnstad, S., Ellingsrud, S., Amundsen, H., Johansen, S., Brevik, I., 2003. A sea bed logging calibration survey over the ormen lange gas field. 65th Ann. Internat. Mtg., Eur. Assoc. Geosc. Eng., Extended Abstracts.

Shanks, W. C. P., Thurston, R., 2012. Volcanogenic massive sulfide occurrence model. U.S. Geological Survey Scientific Investigations Report 2010-5070-C.

Spagnoli, G., Hannington, M., Bairlein, K., Hrdt, A., Jegen, M., Petersen, S., Laurila, T., 2016. Electrical properties of seafloor massive sulfides. An International Journal of Marine Geology 36 (3), 235–245.

Tarantola, A., Valette, B., 1982. Inverse problems = quest for information. Journal of Geophysics 50 (3), 150–170.

Tikhonov, A., Arsenin, V., 1977. Solutions of ill-posed problems. Winston Washington, DC 14.

Um, E. S., Alumbaugh, D. L., 2007. On the physics of the marine controlled-source electromagnetic method. GEOPHYSICS 72 (2), WA13–WA26.

Vozoff, K., 1991. The magnetotelluric method. Electromagnetic Methods in Applied Geophysics: Volume 2, Application, Parts A and B Society of Exploration Geophysicists, 641–712.

Witherly, K., 2012. The evolution of minerals exploration over 60 years and the imperative to explore undercover. The Leading Edge 31 (3), 292–295.

Yang, K., Scott, S. D., 1994. Possible contribution of a metal-rich magmatic fluid to a sea-floor hydrothermal system. Nature 383 (6599), 420.

Zhang, P., King, A., Watts, D., 1998. Using magnetotellurics for mineral exploration. SEG Technical Program Expanded Abstracts 1998, 776–779.

Zhdanov, M. S., 2009. Geophysical Electromagnetic Theory and Methods. Elsevier.

Appendix

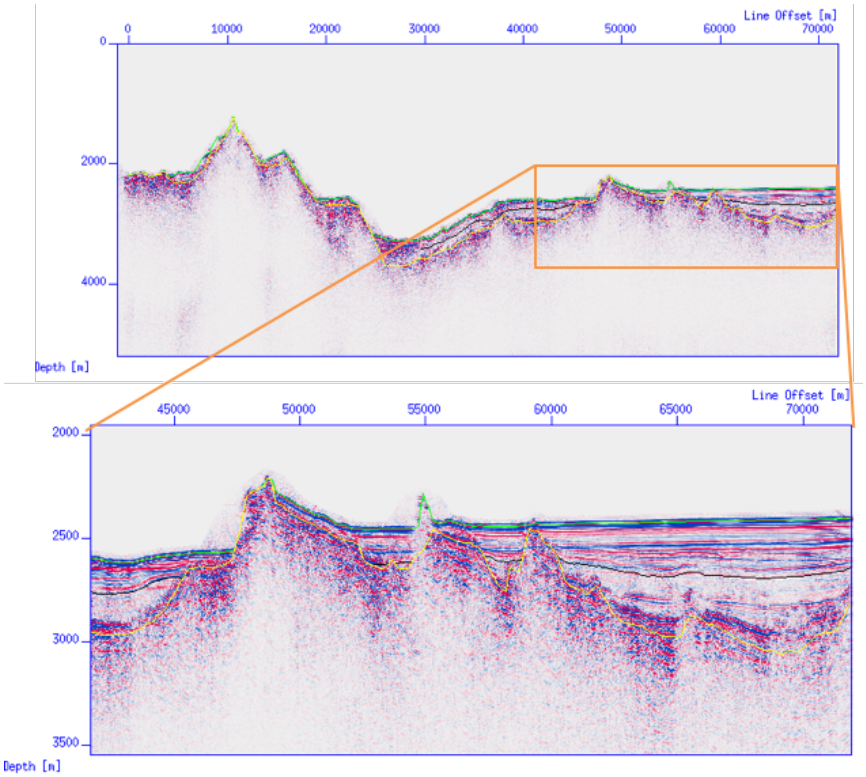

Figure A.1: The location of where the CSEM modelling and inversion of SMS deposits was done showed on the seismic line.

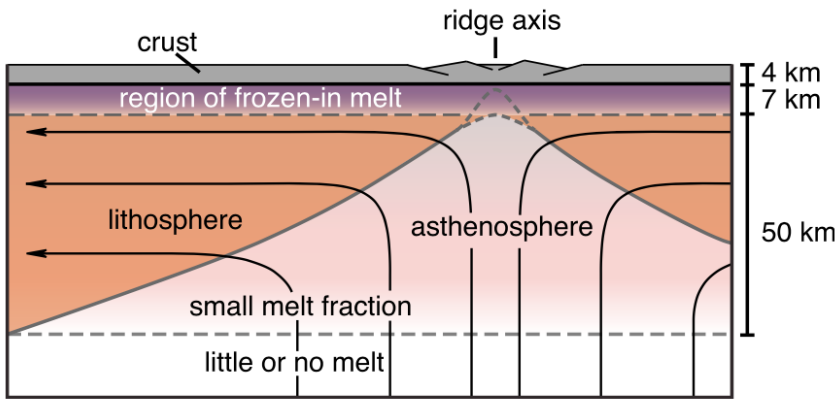

Figure A.2: Cartoon of how Mohns ridge mantle seismic structure. (Conley and Dunn, 2011)